AD-766 048

A STUDY OF THE DYNAMIC STRENGTH AND
FRACTURE PROPERTIES OF ROCK

James Lankford, et al

Southwest Research Institute

Prepared for:

Advanced Research Projects Agency
Bureau of Mines

August 1973

A STUDY OF THE DYNAMIC STRENGTH AND FRACTURE PROPERTIES OF ROCK

by

J. Lankford
W. L. Ko
U. S. Lindholm

FINAL REPORT

Contract No. H0220063
Program Code No. 2F10
SwRI Project 02-3395

Sponsored by

Advanced Research Projects Agency
Monitored by
Bureau of Mines

August 1973

SOUTHWEST RESEARCH INSTITUTE
SAN ANTONIO   CORPUS CHRISTI   HOUSTON

103

DOCUMENT CONTROL DATA - R & D

(Security classification of title, body of abstract and indexing annotation must be entered when the overall report is classified)

1 ORIGINATING ACTIVITY (Corporate author)	2a. REPORT SECURITY CLASSIFICATION
Southwest Research Institute 8500 Culebra Road San Antonio, Texas 78284	Unclassified
	2b. GROUP

3 REPORT TITLE

A STUDY OF THE DYNAMIC STRENGTH AND FRACTURE PROPERTIES OF ROCK

4 DESCRIPTIVE NOTES (Type of report and inclusive dates)

Final Report, May 1972 - September 1973

5 AUTHOR(S) (First name, middle initial, last name)

James Lankford, William L. Ko, and Ulric S. Lindholm

6 REPORT DATE	7a. TOTAL NO OF PAGES	7b. NO. OF REFS
August 1973	99	48

8a. CONTRACT OR GRANT NO H0220063	9a. ORIGINATOR'S REPORT NUMBER(S)
b. PROJECT NO ARPA Order No. 1579, Amendment 3	SwRI 02-3395
c. Program Code No. 2F10	9b. OTHER REPORT NO(S) (Any other numbers that may be assigned this report)
d.	

10 DISTRIBUTION STATEMENT

Distribution of this document is unlimited.

11 SUPPLEMENTARY NOTES	12 SPONSORING MILITARY ACTIVITY
	Advanced Research Projects Agency Bureau of Mines

13 ABSTRACT

This report summarizes the results of a study aimed at developing a quantitative failure strength criterion for Dresser basalt, as well as gaining better understanding of the basic fracture mechanisms involved in fracture. Tests were performed over a temperature range of 77-1400°K, a strain rate range of $10^{-4}-10^3$ sec^{-1}, pressures of 0-100 KSI, and under a variety of uniaxial and biaxial stress states. Failure theories were analyzed, and microfracture was studied extensively. The test results showed that strength to failure data were temperature and strain rate dependent and could be described by a thermally-activated-process relationship. The activation energy was low and appeared to be associated with stress-corrosion assisted cleavage of transgranular cracks. The failure surface was best described by the three-parameter failure criterion of Mogi.

Details of illustrations in
this document may be better
studied on microfiche.

DD FORM 1473
1 NOV 65

i

| 14 KEY WORDS	LINK A		LINK B		LINK C	
	ROLE	WT	ROLE	WT	ROLE	WT
Rock Mechanics						
Basalt						
Multiaxial Stress						
Failure Criteria						
Microcracking						
Thermally-Activated Processes						
High Temperature Testing						

ia

SOUTHWEST RESEARCH INSTITUTE
Post Office Drawer 28510, 8500 Culebra Road
San Antonio, Texas 78284

A STUDY OF THE DYNAMIC STRENGTH AND FRACTURE PROPERTIES OF ROCK

by
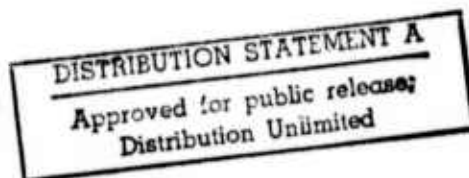J. Lankford
W. L. Ko
U. S. Lindholm

FINAL REPORT

Contract No. H0220063
Program Code No. 2F10
SwRI Project 02-3395

D D C

SEP 10 1973

C
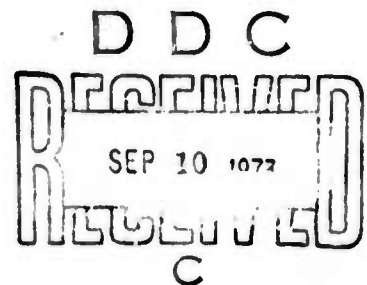
Sponsored by

Advanced Research Projects Agency
Monitored by
Bureau of Mines

August 1973

Approved:

Ulric S. Lindholm, Director
Department of Materials Sciences

ib

ARPA Order Number: 1579
Amendment 3

Program Code Number: 2F10

Name of Contractor:
Southwest Research Institute

Effective Date of Contract:
May 11, 1972

Contract Expiration Date:
September 20, 1973

Amount of Contract: $75,170

Contract Number: H0220063

Principal Investigator and
Phone Number:
U. S. Lindholm
512/684-5111

Project Engineer and Phone
Number:
J. Lankford
512/684-5111

Short Title of Work:
A Study of the Dynamic Strength
and Fracture Properties of Rock

FINAL REPORT

SUMMARY

The general objective of this study has been to develop a quantitative criterion describing the failure strength of hard rock (Dresser basalt), and to attempt to gain an understanding of the fundamental fracture mechanisms responsible for failure. Tests have been performed under a wide range of temperatures (77-1400°K), strain rates ($10^{-4} - 10^3$ sec^{-1}), pressures (0 - 100 KSI), and stress states (uniaxial tension and compression, various biaxial). Various failure theories were analyzed, and extensive microscopic study of microcracking was carried out. Principal conclusions were the following:

1. The strength data may be correlated with a failure criterion which incorporates both temperature and strain rate.[1]

2. One-, two-, three- and four-parameter limit surfaces for isotropic brittle materials have been discussed in detail and presented geometrically in principal stress space. For Dresser basalt, the Mogi three-parameter limit surface seems to fit the overall failure strength data reasonably well.

3. There appear to be at least two energy absorption mechanisms involved in failure of basalt. A thermally-controlled critical stress range exists, above which energy lost through microcracking increases rapidly with stress.

4. Cracks initiate at very low stresses. They initiate and propagate in a transgranular fashion, and propagation usually is possible only for those cracks in a near-axial orientation. Cracks often form en echelon before coalescing into a fault.

5. Failure is thermally activated, with a small activation energy of only 2.6 kcal/mole. The thermally activated process appears to be stress-corrosion assisted cleavage of axially-oriented cracks.

6. Dresser basalt softens at a temperature of about $1400^{\circ}K$.

ACKNOWLEDGMENTS

TABLE OF CONTENTS

Preceding page blank

LIST OF ILLUSTRATIONS

LIST OF ILLUSTRATIONS (Cont'd)

LIST OF ILLUSTRATIONS (Cont'd)

INTRODUCTION

The need for a physically realistic, unified, and general criterion for describing the failure of hard rock under a wide range of temperatures, strain rates, pressures, and stress states is well established, and has been discussed earlier.[1] Current efforts in the areas of excavation, drilling, creep, and explosive loading present problems whose solutions are based on knowledge of response of rock masses under combinations of the above parameters. Unfortunately, much previous research has dealt with only certain specific aspects of rock deformation, making it difficult to formulate a cohesive analytic picture of generalized deformation for a given rock type. The aim of the present effort has been to perform whatever experiments seemed to be needed in order to describe rather completely the regime of failure for Dresser basalt, a representative fine-grained, hard rock. Before discussing the research which was performed, it is useful to review certain earlier work by others which is relevant to the procedures, theories, and conclusions involved in the present study.

As previously discussed, much work has been done in the area of strength properties of rock during isothermal tests at relatively static testing rates. Paul[2] has reviewed various macroscopic criteria for flow and fracture of brittle materials, and a review of the specific work in this area applicable to the present problem is presented as an introduction to the section entitled "Theoretical Analysis of Failure Surfaces."

Only two earlier works have dealt extensively with the temperature-dynamic strain rate dependence of failure in hard rock. In particular, Serdengecti and Boozer[3] and Kumar[4] have shown, for Pala gabbro and basalt, respectively, the equivalence between strain rate and temperature in controlling strength to failure. Other workers, including Green and Perkins,[5] Perkins, et al.,[6] and Brown, et al.,[7] have studied and verified the strong dependence of strength upon strain rate alone during isothermal tests of various rocks. Conversely, creep experiments (Misra and Murrell,[8] Rummel,[9] and Eaton[10]) have provided insight into the thermally activated processes in hard rock controlling isostatic strength at higher temperatures. No dynamic tests have previously been run into this range, i.e., near the melting or softening points.

The studies above generally have dealt with measured deformation or gross failure caused by imposed experimental conditions, and have not involved detailed microscopic examination of the fracture processes occurring during the deformation. Other workers have been more concerned with this aspect of the problem.

In 1964, Brace[11] considered the stress-strain curve for rocks, and showed that it generally could be divided into four distinct regions. He concluded that within the third region, defined by initial deviation of the curve from elasticity, cracks formed at grain boundaries, or pre-existing grain boundary cracks started to grow, and these ultimately led to failure (the fourth region) through intergranular fracture. Subsequently, Brace,

2

Paulding, and Scholz[12] showed that volumetric dilatancy could be related to the formation of axial cracks during compression. Scholz[13, 14] independently related the microfracturing within Region III to subsequent fault formation and failure, using acoustic emission techniques. His results also indicated (indirectly) that failure during creep and failure during constant strain rate tests appear to be caused by similar microfracturing mechanisms. Other results predicted[15] and showed[16] the profound control over fracture strength during creep attributable to the environment, especially the water content. By implication, a similar effect should exist for constant strain rate tests. This supposition was backed up by the work of Krokosky and Husak,[17] who an air and vacuum environment tests under constant strain rate conditions, and achieved differences in strength of a factor of two. On the other hand, some doubt as to the validity of the idea of grain boundary cracking as the origin of dilatancy and microfracture-induced failure has arisen as a result of the recent work of several experimenters. Wawersik,[13] Peng,[19] Friedman, et al.,[20] and Wawersik and Brace[21] all show a predominance of intracrystalline, not intergranular, cracks parallel to the axis of compression in rocks above ~60% of the fracture strength. The SEM work of Brace, et al.,[22] supports these observations, to the extent that initial grain boundary flaws resemble pores with rounded ends, rather than "sharp" Griffi h cracks. Still, it has not yet been established whether the initial cracks which form, and possibly control, subsequent crack initiation and growth, are intragranular or intergranular.

3

EXPERIMENTAL PROCEDURES

Rock Petrography

As discussed in a previous report,[1] Dresser basalt is a dark grayish green, massive, fire-grained hard rock. Recent analysis[23] at the Twin Cities BuMines laboratories indicates that the principal constituents are feldspar (41%) and pyroxene (40%). Wavelength dispersive X-ray microanalysis carried out at SwRI during the second year of the project agrees closely with this analysis. Mineral constituents will be discussed further in terms of microcracking mechanisms.

Specimen Preparation

A number of special specimen configurations were required during the course of the project, in order to provide access to certain regions of stress-space. Earlier, conventional cylindrical specimens (Figure 1a) were used in confined and unconfined uniaxial compression, and in the latter case, temperature and strain rate were varied. However, this specimen design does not allow the generation of biaxial or tensile stress states.

Therefore, for tensile testing, "dumbbell"-shaped specimens were machined to the dimensions shown in Figure 1b. In addition, hollow, cylindrical specimens of reduced cross-sectional area (Figure 1c), primarily intended for biaxial testing (compression-torsion and tension-torsion), were used for pure tension testing. These different specimen designs

4
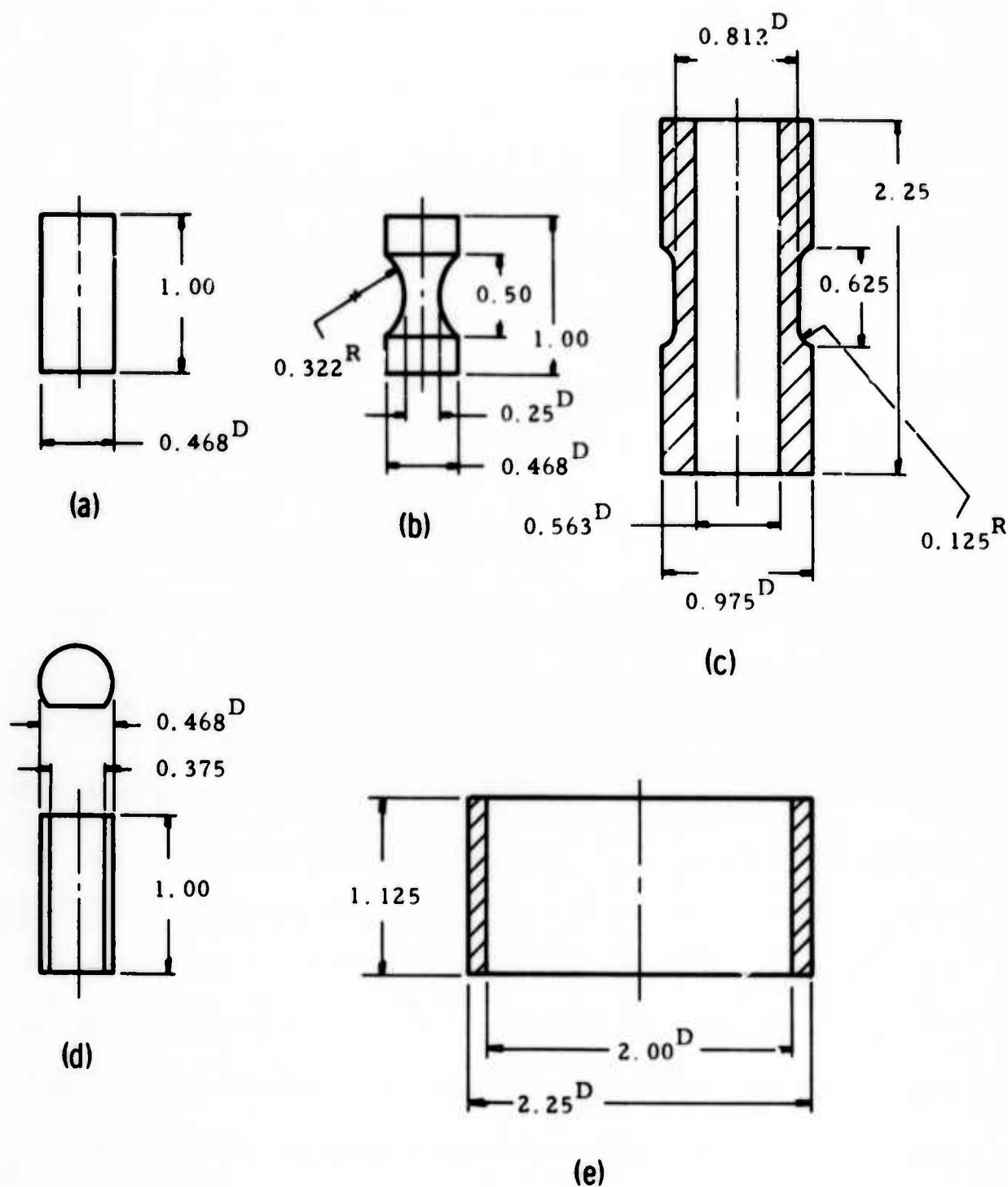
FIGURE 1. SPECIMEN CONFIGURATIONS

provided a check as to the influence of geometry and grip constraint upon nominally identical stress-states.

Other tests required axial compression combined with either internal or external pressure. Therefore, ring-shaped specimens of the configuration drawn in Figure 1e were fabricated.

It is extremely difficult to observe crack development on the surfaces of specimens finished only for testing, since surface roughness conceals the cracks. Consequently, several of the solid cylindrical specimens were modified as an aid in the study of sequential microcrack formation. In particular, a flat was ground onto each of these cylinders, as shown in Figure 1d, and the flats were lapped to an extremely smooth surface. The surface proved ideal for surface replication techniques.

Test Procedures

Most aspects of the experimental program have been covered fully in previous reports,[1, 24, 25] especially the multi-strain rate, high-pressure facility. However, certain aspects of the current work have not yet been discussed, in particular the biaxial testing facility, the high-temperature facility, and the procedures followed in running hysteresis loss experiments, strain distribution tests, and creep tests. Replication techniques also have only recently been employed. All of these will be considered below.

The biaxial testing facility (Figure 2) has three alternate modes of biaxial loading: (1) either axial tension/compression and torsion; (2) axial

6

INTERNAL PRESSURE
INTENSIFIER

HYDRA[...]
POWER[...]

SPECIMEN

TORSIONAL
ACTUATOR

LINEAR
ACTUATOR

LOAD FRAME

CONTROL
SYSTEM

RECORDING
INSTRUMENTATION
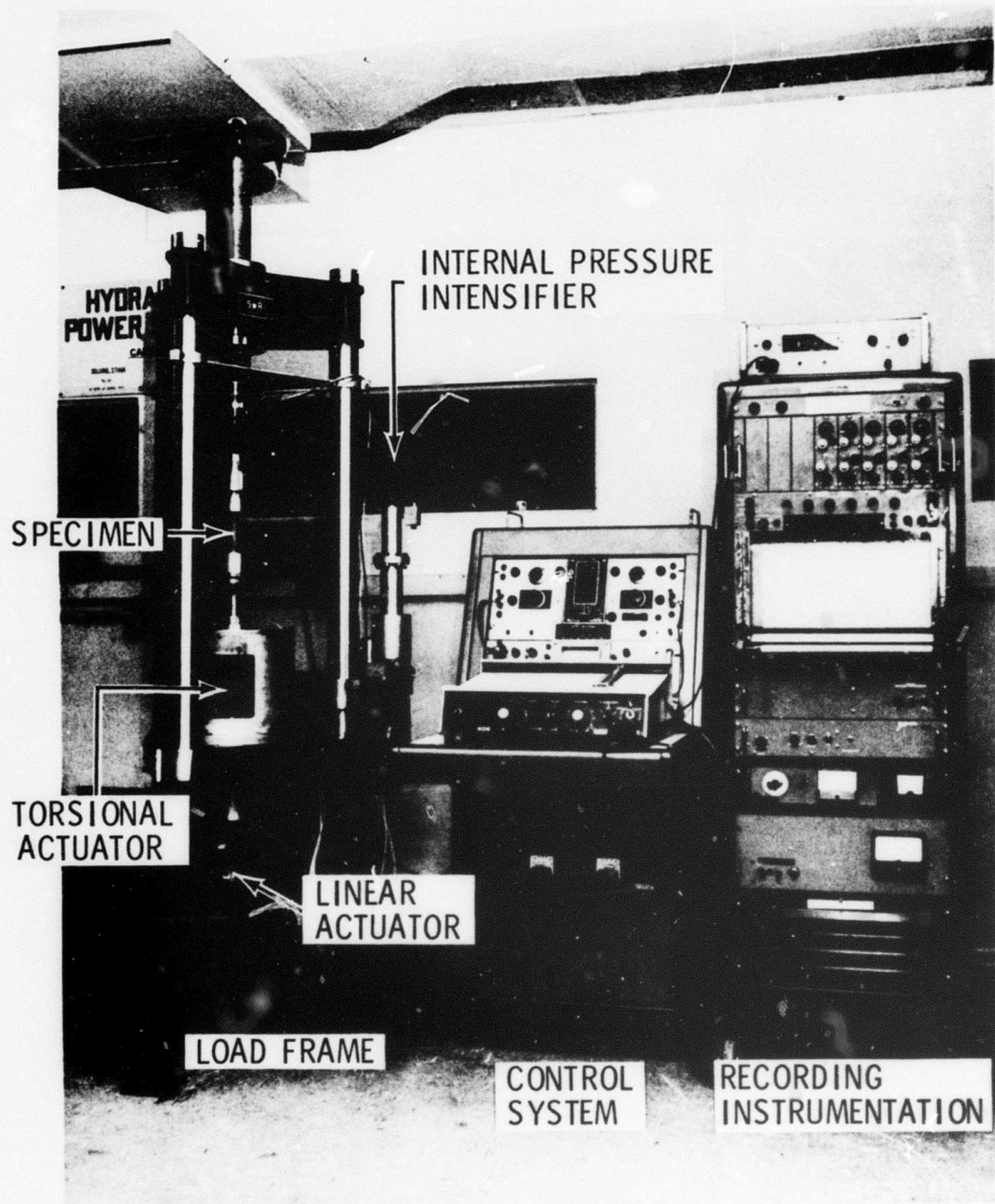
FIGURE 2.   OVERALL VIEW OF THE SwRI MULTIAXIAL
TESTING FACILITY

tension/compression and internal pressure; or (3) axial tension/compression and external pressure, using a high-pressure bomb (not shown but discussed previously[1]). Specimens are of thin-walled tubular geometry, as discussed in the preceding section. Each load function operates from an independent hydraulic actuator and control system. Thus, each load component is independently programmable, allowing an infinite variation in load ratio. The machine will, of course, operate in a uniaxial mode as well, and can be programmed for repeated (fatigue) loadings.

One of the biaxial machines recently has been equipped for uniaxial compression testing at high temperatures. In particular, a Marshall filament-wound (Pt-20% Rh) furnace, capable of attaining 1600°K, was fitted into the load frame. The thermal gradient was minimized by increasing the winding density near the furnace ends. For load application within the hot zone, special ultra-high purity alumina rods were used, coupled to water-cooled stainless steel loading fixtures (Fig. 3).

Hysteresis energy loss was measured by running uniaxial load-unload cycles, using strain-gaged specimens, at successively higher stress levels until failure. Closed hysteresis loops (Figure 4) were thereby obtained, each of whose area ($\oint \sigma \, d\epsilon$) is equal to the irreversible energy ΔE lost to inelastic flow during a given cycle. Areas were measured using a planimeter. The data are presented as plots of ΔE versus σ, and are discussed later. Low-temperature data were obtained by immersion of the

8
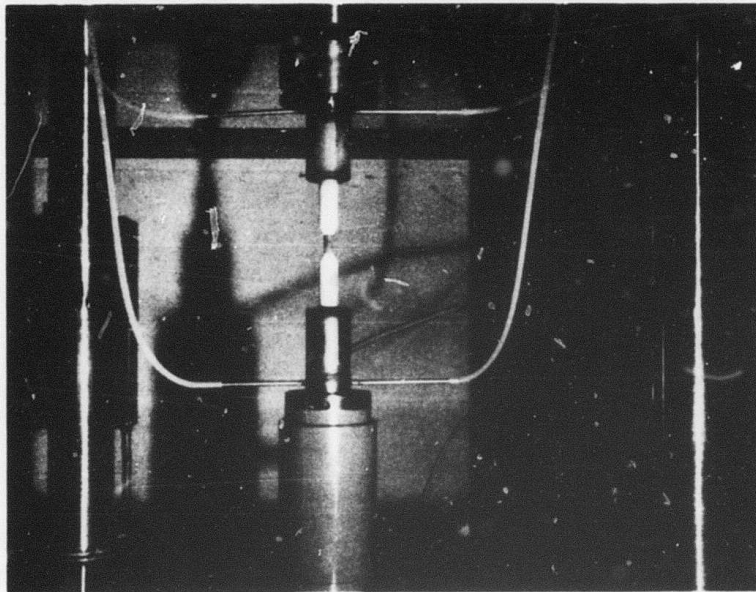
FIGURE 3.   HIGH TEMPERATURE UNIAXIAL
COMPRESSION FACILITY
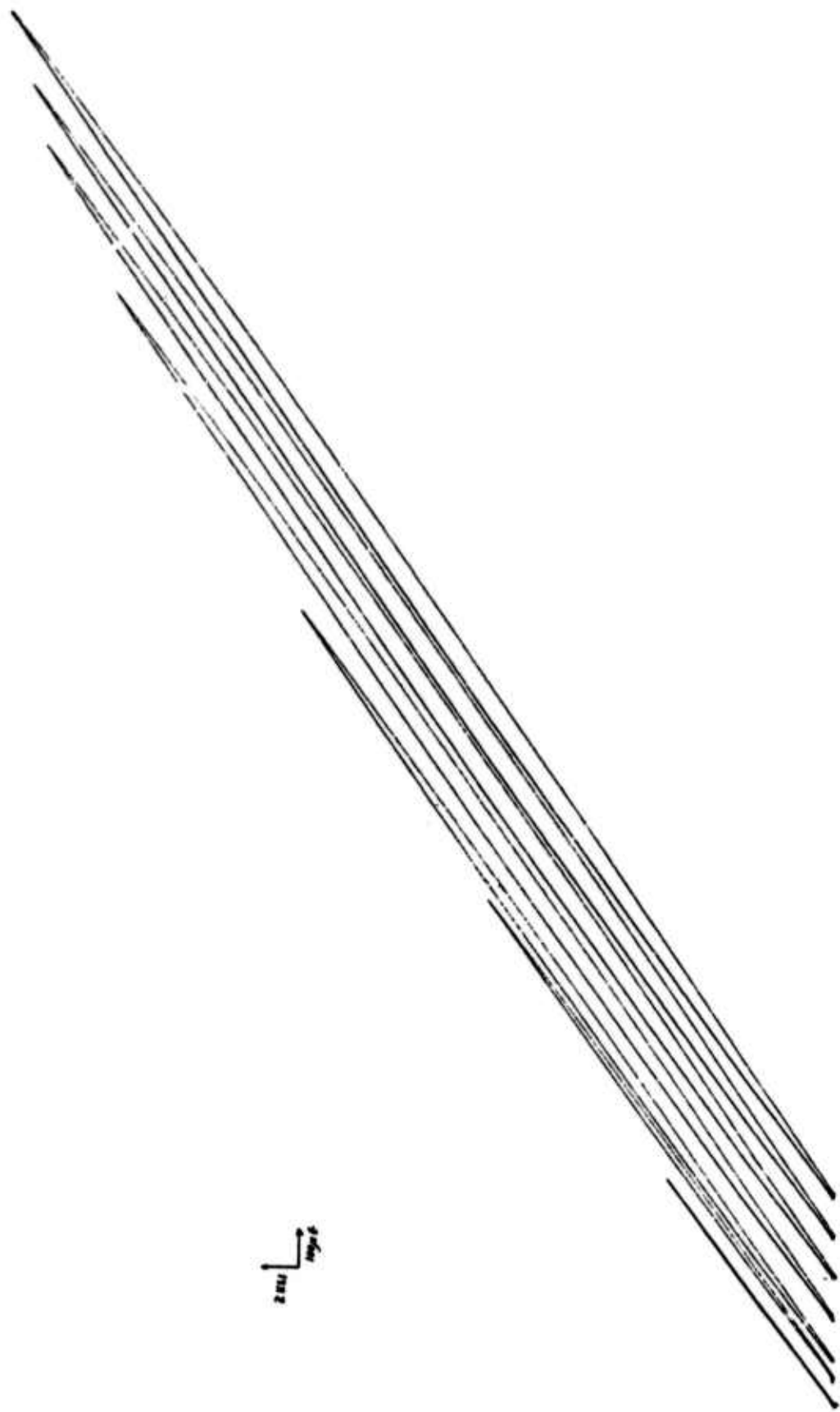
FIGURE 4. TYPICAL HYSTERESIS LOOPS (300°K)

10

specimen and loading anvils in liquid nitrogen during testing. Specimens were instrumented with both longitudinal and circumferential strain gages, so that volumetric changes might be monitored as well. It should be pointed out that the circumferential gages used in these particular tests had a gage length of only 0. 125 in., so that the "dilatancy" measured here was extremely localized, hence unlikely to reflect the very large net volume increases observed, near failure, by certain other investigators. The gages were not compensated for temperature, since thermal fluctuations would constitute a minor effect.

A number of creep tests were run in which cylindrical specimens were loaded in uniaxial compression at a strain rate of $1. 9 \times 10^{-1}$ to various stress levels within the failure stress scatterband for specimens failed in uniaxial compression of $1. 9 \times 10^{-4} sec^{-1}$, and then held until failure. Time to failure was monitored, and the times were then compared with the failure times of the specimens compressed to failure at the slow strain rate.

In studying microcrack initiation and growth, the following procedure was used. Prior to loading, replicas of the undeformed smooth, flat face were taken using Bioden replicating tape capable of recording detail on the order of 50 $\overset{o}{A}$. The specimen was then loaded in incremental stress steps to failure, i.e., formation of a crack of the order of size of the specimen. At each step, replicas were taken in the loaded and unloaded state, or in the unloaded state alone. The latter was generally necessary, since the specimen tended to creep to failure if held at a high load during replication. The

11

replicas were then examined, without coating, using optical and scanning electron microscopy (SEM). Optical study using Nomarski interference was especially fruitful. Actual failed specimens have been studied in the SEM, and electron spectroscopic analysis used to help determine the mineral constituents in which fracture initiated.

It was of interest to know whether strain was generally homogeneous within the various specimen configurations. With this goal in mind, some of both the solid cylindrical specimens and the hollow ring specimens (Fig. 1, a and e) were instrumented with circumferential strain gages, which were monitored as the specimens were loaded elastically. In the case of the hollow rings, several loading paths ranging from pure axial to pure radial compression were run, including combined loadings. For most of these tests, several strain gages were placed end to end in a circumferential pattern, so that almost the total circumferential strain was measured.

THEORETICAL ANALYSIS OF FAILURE SURFACES

Introduction

In order to predict the strength (yield or failure) of materials, establishment of strength theories is necessary. In the formulation of empirical strength theories, it is assumed that there exists a limit surface, and the strength parameters in the limit surface equation (strength criterion) are determined by conducting tests in simple stress fields. The applicability of the postulated strength criterion is checked by running tests in other stress fields. In the formulation, the limit surface equation should be as simple as possible and must satisfy the principle of objectivity.

Limit surfaces of common ductile materials are well established, and much has been published on this subject.[2] The most notable and widely accepted limit surfaces in stress space are the Tresca and Von Mises limit surfaces for isotropic ductile materials.[2,26] On the other hand, for brittle isotropic materials (e.g., rocks) or anisotropic materials (e.g., fiber-reinforced composites), the forms of limit surfaces still are not very well understood. Various strength theories for anisotropic materials recently have been reviewed by Sendeckyj[27] and Priddy,[28] and interesting photographs of three-dimensional models of some simple limit surfaces in principal stress space have been shown by Mehldahl.[29] Most of the strength theories proposed for brittle materials are generalizations

13

or extrapolations from distortional energy theory, or are the generalization or modification of Tresca's theory.

The purpose of this section is to review some major failure theories which might be applicable to isotropic brittle materials, and to present the geometry of the limit surface associated with each theory in three-dimensional principal stress space, for quick visualization.

Failure Criteria

The most general form of limit surface equation in terms of stresses[*] for arbitrary materials can be represented by the following scalar series equation which is invariant with respect to the coordinate transformations[31]

$$f(\sigma_{rs}) = (A_{ij}\sigma_{ij})^{\alpha} + (B_{ijk\ell}\sigma_{ij}\sigma_{k\ell})^{\beta} + (C_{ijk\ell mn}\sigma_{ij}\sigma_{k\ell}\sigma_{mn})^{\gamma} \qquad (1)$$
$$+ \ldots = 1$$

where A_{ij}, $B_{ijk\ell}$, $C_{ijk\ell mn}$,... are respectively the second, the fourth, the sixth,.... rank strength tensors, and α, β, γ,.... are constants. When $\alpha = \beta = \gamma = \ldots = 1$, Equation (1) reduces to the Malmeister equation.[32]

All the failure criteria to be discussed are special cases of the general Equation (1). Since only isotropy is concerned, all the limit surfaces in the principal stress space will have trigonal symmetry with respect to the space diagonal of principal stress space.

In plotting the limit surfaces in principal stress space $\{\sigma_1, \sigma_2, \sigma_3\}$, it is more convenient to transform the $\{\sigma_1, \sigma_2, \sigma_3\}$ system to the

---

[*] Failure theories may also be formulated in terms of strains, especially for large deformations.[30]

14

$\{\sigma_1^*, \sigma_2^*, \sigma_3^*\}$ system shown in Figure 5, where σ_1^* lies parallel with the intersection of the $\sigma_1\sigma_2$-plane with the π-plane and passes through the origin, σ_2^* lies in the same π-plane, with equal inclination to the σ_1 and σ_2 axes, and σ_3^* coincides with the $\sigma_1 = \sigma_2 = \sigma_3$ space diagonal of the $\{\sigma_1, \sigma_2, \sigma_3\}$ system.[†] The relationship between the two systems is given below.

$$\sigma_1 = \frac{1}{\sqrt{6}} \left(\sqrt{3}\, \sigma_1^* + \sigma_2^* + \sqrt{2}\, \sigma_3^* \right) \tag{2}$$

$$\sigma_2 = -\frac{1}{\sqrt{6}} \left(\sqrt{3}\, \sigma_1^* - \sigma_2^* - \sqrt{2}\, \sigma_3^* \right) \tag{3}$$

$$\sigma_3 = -\frac{1}{\sqrt{3}} \left(\sqrt{2}\, \sigma_2^* - \sigma_3^* \right) \tag{4}$$

or

$$\sigma_1^* = \frac{1}{\sqrt{2}} \left(\sigma_1 - \sigma_2 \right) \tag{5}$$

$$\sigma_2^* = \frac{1}{\sqrt{6}} \left(\sigma_1 + \sigma_2 - 2\sigma_3 \right) \tag{6}$$

$$\sigma_3^* = \frac{1}{\sqrt{3}} \left(\sigma_1 + \sigma_2 + \sigma_3 \right) \tag{7}$$

In the following we will discuss one-, two-, three- and four-parametric failure criteria and the associated limit surfaces. The validity of each theory must be examined in the light of experimental data.

One-Parametric Limit Surfaces

The equation of the one-parametric limit surface contains only one strength constant. Therefore, the limit surface can be determined simply by performing a test in a single stress field.

[†] Since the failure criteria relate to materials generally, tension was considered positive, and compression negative. However, for the actual results presented later, the opposite convention was followed, as is the custom in rock mechanics.
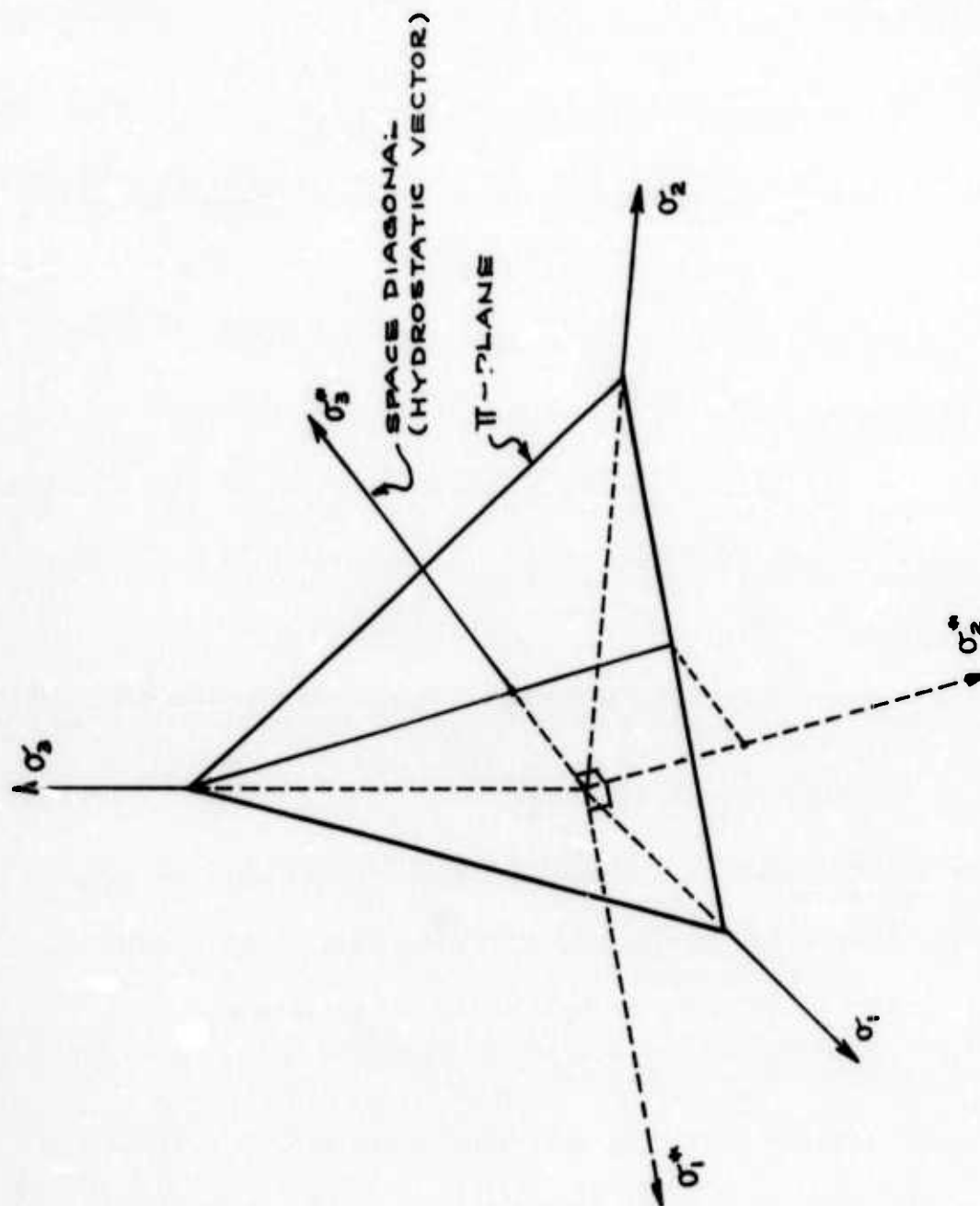
FIGURE 5. STRESS COORDINATES

The most widely used one-parametric limit surfaces are the Tresca and Von Mises limit surfaces, whose equations, written in terms of principal stresses, are:

(1)   Tresca Criterion[2]

$$A (\sigma_i - \sigma_j) = 1 \; ; \; i, j = 1, 2, 3 \tag{8}$$

(2)   Von Mises Criterion[2]

$$A \, II_D = 1 \tag{9}$$

where A is a strength constant and

$$II_D \equiv \sigma_1^2 + \sigma_2^2 + \sigma_3^2 - \sigma_1\sigma_2 - \sigma_2\sigma_3 - \sigma_3\sigma_1$$

$$= \frac{3}{2} (\sigma_1^{*2} + \sigma_2^{*2})$$

$$= 3 \times (\text{Second Deviatoric Stress Invariant}) \tag{10}$$

The geometries of the familiar Tresca and Mises limit surfaces are reproduced in Figure 6 and Figure 7, respectively.

The Tresca limit surface is an infinitely long regular hexagonal prismatic surface coaxial with the space diagonal (or hydrostatic vector). The intersection (or limit focus) of this surface with a coordinate surface is an irregular hexagon which has two interior angles of 90°, and four of 135°. The Tresca criterion states that the maximum shearing stress at failure is independent of both mean normal stress and the third stress σ_k ($k \neq i \neq j$), and thus permits unlimited hydrostatic tensions which are physically unattainable.

17

$$A(\sigma_i - \sigma_j) = 1$$

FIGURE 6. REGULAR HEXAGONAL PRISMATIC LIMIT SURFACE IN PRINCIPAL STRESS SPACE BASED ON TRESCA CRITERION (ONE-PARAMETRIC SURFACE)
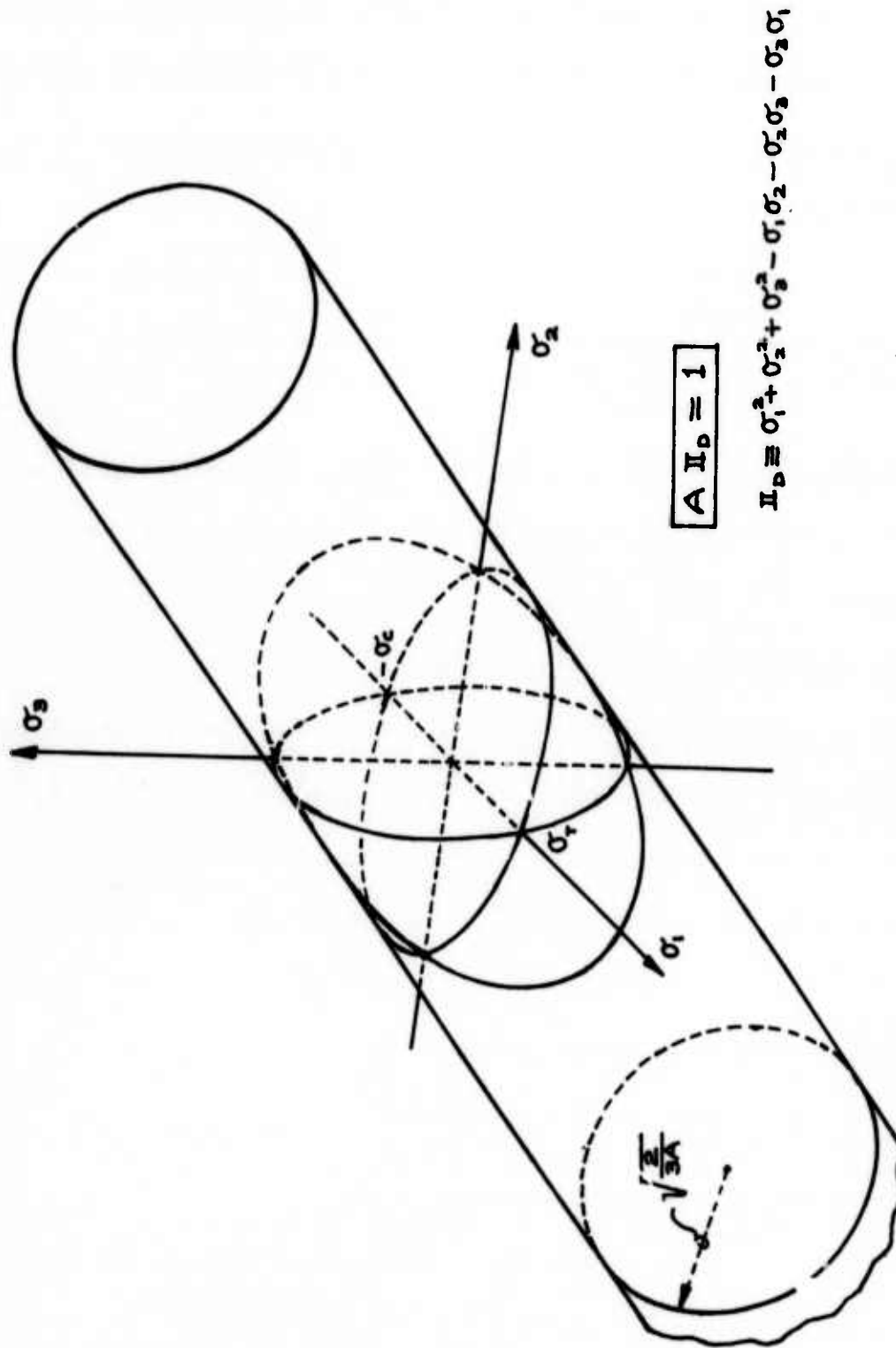
FIGURE 7. CIRCULAR CYLINDRICAL LIMIT SURFACE IN PRINCIPAL STRESS SPACE BASED ON VON MISES CRITERION (ONE-PARAMETRIC SURFACE)

$A \, II_D = 1$

$II_D \equiv \sigma_1^2 + \sigma_2^2 + \sigma_3^2 - \sigma_1\sigma_2 - \sigma_2\sigma_3 - \sigma_3\sigma_1$

19

While the Von Mises limit surface is an infinitely long circular cylindrical surface with radius $\sqrt{\dfrac{2}{3A}}$ coaxial with the space diagonal, the intersection of this surface with a coordinate surface is an ellipse centered at the origin. This criterion states that the ultimate distortional strain energy (or octahedral shearing stress) is not affected by the mean normal stress and also permits unrealistic hydrostatic tensions.

These one-parameter theories are also called symmetrical theories since they predict equal strengths in tension and compression. They are applicable to the yield behavior of most of the isotropic ductile materials.

Two-Parametric Limit Surfaces

The two-parametric failure theories are unsymmetrical in that they predict unequal strengths in tension and compression. There are two adjustable strength constants in the limit surface equation, and therefore tests in two stress fields are necessary in determining the limit surface.

(1)   Coulomb-Mohr Criterion[2]

$$A \, \sigma_i + B \sigma_j = 1 \; ; \; i, j = 1, 2, 3 \tag{11}$$

where A, B are the strength constants.

This criterion is a linear combination of any two principal stresses and is the generalization of the Tresca criterion. The limit surface based on this criterion is an irregular hexagonal pyramid intersecting

20

the positive and negative axes, respectively, at σ_T (ultimate uniaxial tensile stress) and $-\sigma_C$ (ultimate uniaxial compressional stress), as shown in Figure 8. The apex of this pyramid is located on the space diagonal at $\sigma_3^* = \frac{\sqrt{3}}{A+B}$ (or $\sigma_1 = \sigma_2 = \sigma_3 = \frac{1}{A+B}$), hence the criterion predicts finite hydrostatic tensions. It can be seen that shear failure is dependent on the mean normal stress and is completely independent of the intermediate principal stress σ_k ($k \neq i \neq j$). When $A = -B$, the Coulomb-Mohr criterion reduces to the Tresca criterion.

(2) Nadai Criterion[33, 34]*

$$AI + BII_D^{\frac{1}{2}} = 1 \tag{12}$$

or

$$\sqrt{3}\, A \sigma_c^* + \sqrt{\frac{3}{2}}\, B \sqrt{\sigma_1^{*2} + \sigma_2^{*2}} = 1 \tag{13}$$

where

$$I \equiv \sigma_1 + \sigma_2 + \sigma_3 = \sqrt{3}\, \sigma_3^* \tag{14}$$

This criterion postulates that the ultimate octahedral shearing stress is a linear function of the mean normal stress. The limit surface associated with this criterion is a circular cone coaxial with the space diagonal, whose semi-angle ϕ is given by $\tan \phi = \frac{\sqrt{2}\, A}{B}$ (in Figure 9). The apex of this cone is located at $\sigma_3^* = \frac{1}{\sqrt{3}\, A}$ (or $\sigma_1 = \sigma_2 = \sigma_3 = \frac{1}{3A}$), and the radius of a circular contour in the π-plane is $\frac{\sqrt{2}}{\sqrt{3}\, B} (1 - \sqrt{3}\, A \sigma_3^*)$. The

---

*This is a special case of the general form $II_D^{\frac{1}{2}} = f(I)$ suggested by Schleicher.[35]
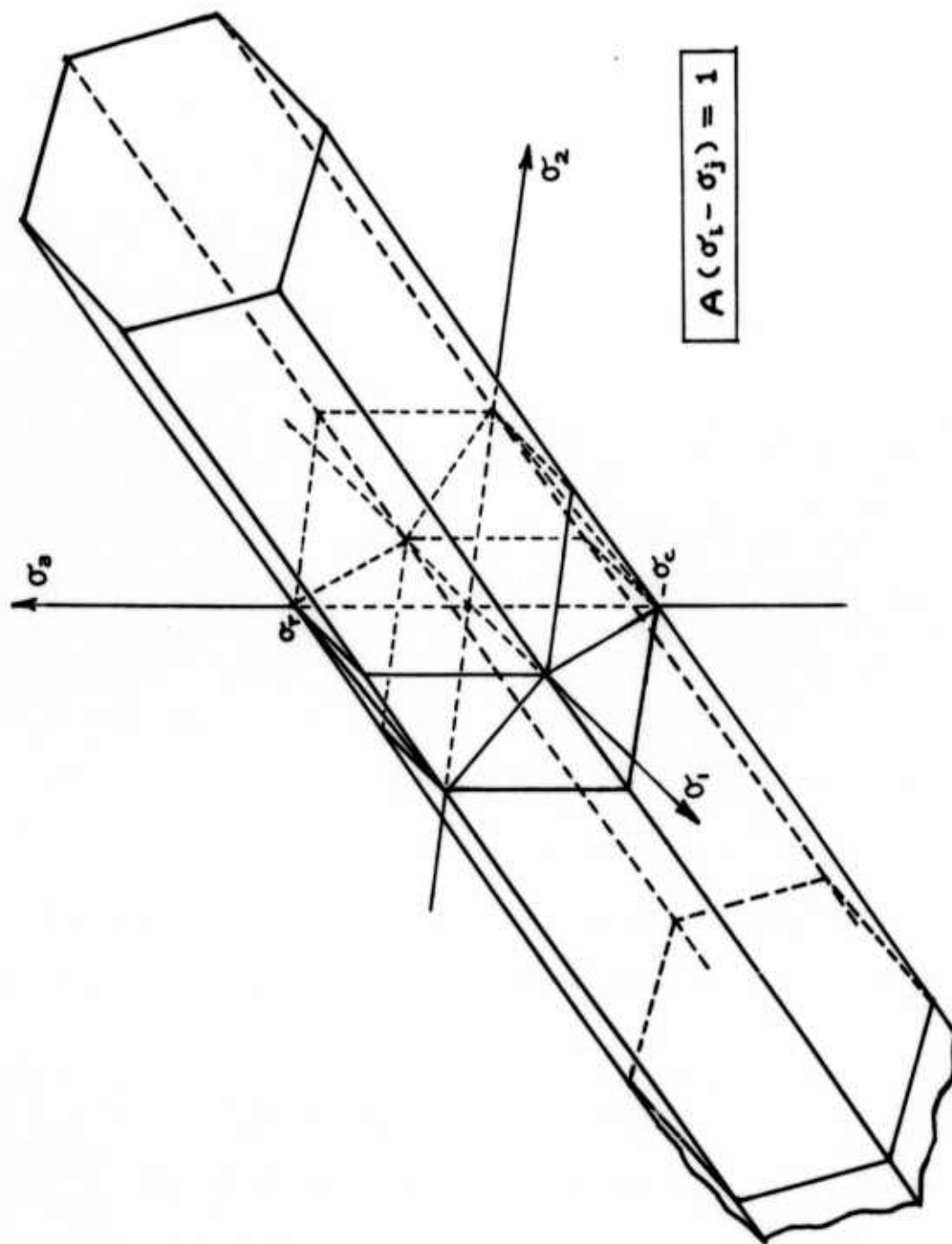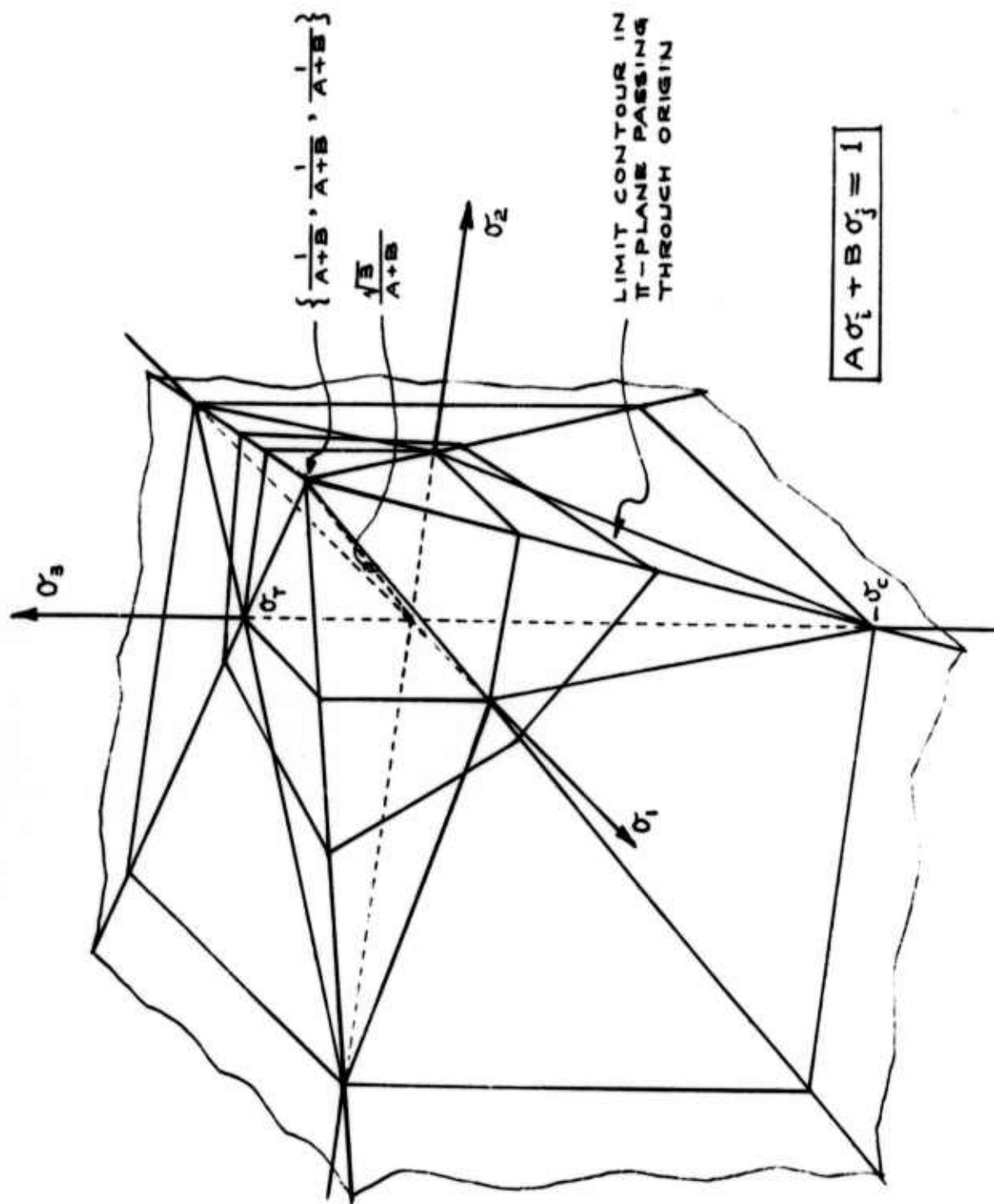
FIGURE 8. IRREGULAR HEXAGONAL PYRAMIDAL LIMIT SURFACE IN PRINCIPAL STRESS SPACE BASED ON COULOMB-MOHR CRITERION (TWO-PARAMETRIC SURFACE)

22
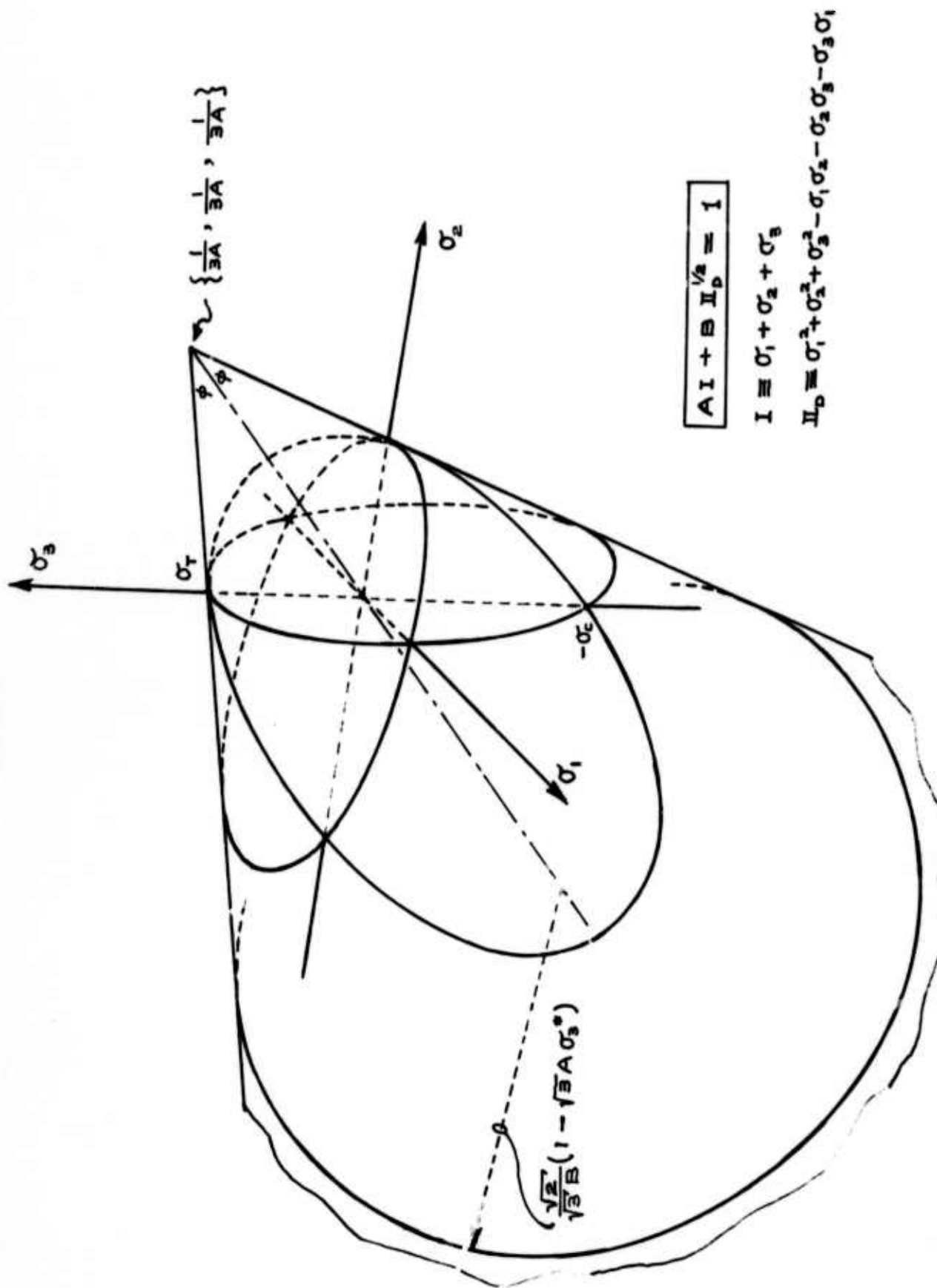
FIGURE 9. CIRCULAR CONICAL LIMIT SURFACE IN PRINCIPAL STRESS SPACE BASED ON NADAI CRITERION (TWO-PARAMETRIC SURFACE)

$$AI + B \, II_D^{1/2} = 1$$

$$I \equiv \sigma_1 + \sigma_2 + \sigma_3$$

$$II_D \equiv \sigma_1^2 + \sigma_2^2 + \sigma_3^2 - \sigma_1 \sigma_2 - \sigma_2 \sigma_3 - \sigma_3 \sigma_1$$

$$\frac{\sqrt{2}}{\sqrt{3} \, B} (1 - \sqrt{3} A \sigma_3^*)$$

23

intersection (limit locus) of the cone with a coordinate plane will be an ellipse if $\dfrac{\sigma_C}{\sigma_T} < 3$, a parabola if $\dfrac{\sigma_C}{\sigma_T} = 3$, and a hyperbola if $\dfrac{\sigma_C}{\sigma_T} > 3$.[36]

When A and B are related to σ_T and σ_C, one has

$$A = \frac{\sigma_C - \sigma_T}{2\,\sigma_T \sigma_C} \tag{15}$$

$$B = \frac{\sigma_T + \sigma_C}{2\,\sigma_T \sigma_C} \tag{16}$$

When $\sigma_T = \sigma_C$, the cone transforms into Mises cylinder, and, therefore, the Nadai criterion may be regarded as a modification of Mises criterion by introducing into it the mean normal stress weighted by A.

(3)   Torre Criterion[37]

$$A I + B II_D = 1 \tag{17}$$

or

$$\sqrt{3}\, A\, \sigma_3^{\,*} + \frac{3}{2} B \,(\sigma_1^{*2} + \sigma_2^{*2}) = 1 \tag{18}$$

This criterion postulates that the ultimate distortional energy is a linear function of the mean normal stress. The limit surface based on this criterion is a paraboloid of revolution coaxial with the space diagonal shown in Figure 10. The vertex of the paraboloid is located at $\sigma_3^{\,*} = \dfrac{1}{\sqrt{3}\,A}$ (or $\sigma_1 = \sigma_2 = \sigma_3 = \dfrac{1}{3\,A}$), and the radius of a circular contour on a π-plane is $\left[\dfrac{2}{3\,B}\,(1 - \sqrt{3}\,A\,\sigma_3^{\,*})\right]^{\frac{1}{2}}$. The intersection of the paraboloid with a coordinate surface is an ellipse. This surface is more appealing because, unlike the

24
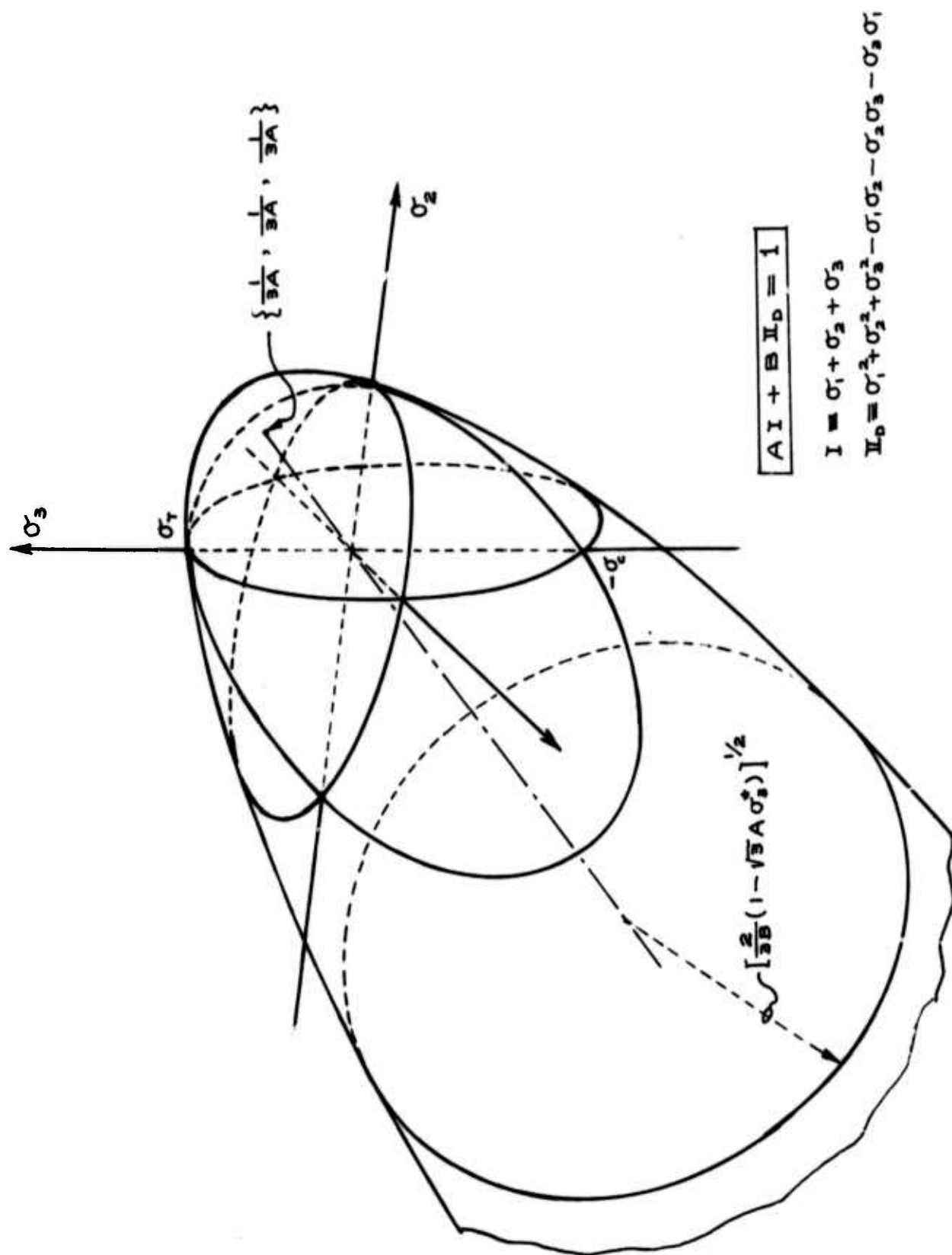
FIGURE 10. PARABOLOID-OF-REVOLUTION LIMIT SURFACE IN PRINCIPAL STRESS SPACE BASED ON TORRE CRITERION (TWO-PARAMETRIC SURFACE)

25

cone, it does not have a physically unrealistic sharp apex in the first octant

of the principal stress space. When A, B are related to σ_T, σ_C, we have

$$A = \frac{\sigma_C - \sigma_T}{\sigma_T \sigma_C} \tag{19}$$

$$B = \frac{1}{\sigma_T \sigma_C} \tag{20}$$

When $\frac{\sigma_C}{\sigma_T} \longrightarrow \infty$, we have $A \longrightarrow \frac{1}{\sigma_T}$, $B \longrightarrow 0$, and Equation (17) becomes

$$I = \sigma_T \tag{21}$$

so that the paraboloid degenerates into the principal octahedral plane. When

$\sigma_T = \sigma_C$, the paraboloid, just like the cone, transforms into the Mises cyl-

inder.

(4)   Sobotka Criterion[38]

$$A II_D + B III_D = 1 \tag{22}$$

or

$$\frac{3}{2} A (\sigma_1^{*2} + \sigma_2^{*2}) + \frac{3\sqrt{6}}{2} B \sigma_2^* (3\sigma_1^{*2} - \sigma_2^{*2}) = 1 \tag{23}$$

where

$$III_D \equiv 2 (\sigma_1^3 + \sigma_2^3 + \sigma_3^3) - 3 (\sigma_1^2 \sigma_2 + \sigma_1^2 \sigma_3 + \sigma_2^2 \sigma_1 + \sigma_2^2 \sigma_3$$

$$+ \sigma_3^2 \sigma_1 + \sigma_3^2 \sigma_2) + 12 \sigma_1 \sigma_2 \sigma_3$$

$$= 27 \times \text{(Third Deviatoric Stress Invariant)} \tag{24}$$

26

This theory postulates that the ultimate distortional energy depends linearly on the third deviatoric stress invariant. The limit surface of this theory, shown in Figure 11, consists of one prismatic surface coaxial with the space diagonal, whose cross section is a three-lobed figure, and three open-channeled surfaces parallel to the prism and located at trigonally symmetric positions. The existence of these open channel surfaces arises from the cubic nature of the limit surface equation. The purpose of including the III_D term is to distort the Mises circle into the three-lobed figure; however, the three open-channeled surfaces should be disregarded in terms of physical significance. The two strength constants A and B, when written in terms of σ_T and σ_C, have the forms

$$A = \frac{\sigma_T^2 - \sigma_T \sigma_C + \sigma_C^2}{\sigma_T^2 \sigma_C^2} \tag{25}$$

$$B = \frac{\sigma_C - \sigma_T}{2 \sigma_T^2 \sigma_C^2} \tag{26}$$

For large $\dfrac{\sigma_C}{\sigma_T}$, the convex three-lobed figure of the prism may form a tri-star shape, the three innermost regions of which will be concave. This is not a reasonable description of the yielding of stable work-hardening materials.[39] However, for fracture rather than plastic flow, there may well exist materials which are not stable work-hardening in the sense of Drucker.[39]

27

$$\boxed{A\,\mathrm{II}_D + B\,\mathrm{III}_D = 1}$$

$$\mathrm{II}_D = \sigma_1'^2 + \sigma_2'^2 + \sigma_3'^2$$
$$\quad - \sigma_1'\sigma_2' - \sigma_2'\sigma_3' - \sigma_3'\sigma_1'$$

$$\mathrm{III}_D = 2\,(\sigma_1'^3 + \sigma_2'^3 + \sigma_3'^3)$$
$$\quad - 3\,(\sigma_1'^2\sigma_2' + \sigma_1'^2\sigma_3'$$
$$\quad + \sigma_2'^2\sigma_1' + \sigma_2'^2\sigma_3'$$
$$\quad + \sigma_3'^2\sigma_1' + \sigma_3'^2\sigma_2')$$
$$\quad + 12\,\sigma_1'\sigma_2'\sigma_3'$$

CONTOUR LINES IN A π-PLANE

σ_2

σ_3

σ_1

σ_t

$-\sigma_c$
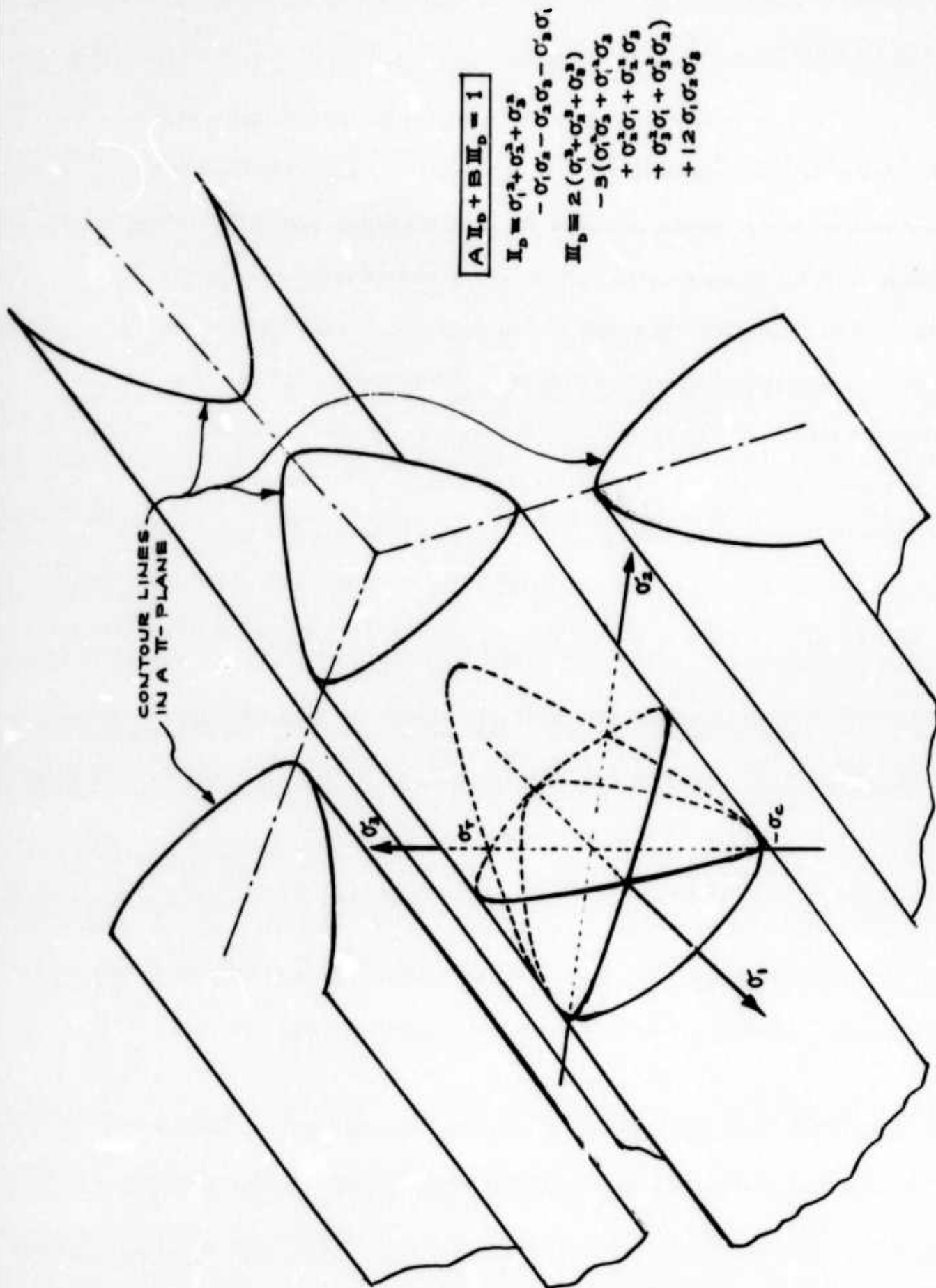
FIGURE 11. PRISMATIC CUBIC LIMIT SURFACE IN PRINCIPAL STRESS SPACE BASED ON SOBOTKA CRITERION (TWO-PARAMETRIC SURFACE)

28

Three-Parametric Limit Surfaces

Applicability of the one- and two-parametric theories may be limited because of an insufficient number of adjustable constants. The three parametric theories give additional degrees of freedom in generating refined limit surfaces.

(1) Paul-Haythornthwaite Criterion[2]

$$A\sigma_i + B\sigma_j + C\sigma_k = 1 \quad ; \quad i, j, k = 1, 2, 3 \tag{27}$$

where A, B, C are the three strength constants.

This criterion is a linear combination of the three principal stresses. The limit surface of Equation (27) is an irregular hexagonal pyramid coaxial with the space diagonal (generalized Coulomb-Mohr pyramid), and whose apex is located on the space diagonal at $\sigma_3^* = \frac{\sqrt{3}}{A+B+C}$ (or $\sigma_1 = \sigma_2 = \sigma_3 = \frac{1}{A+B+C}$) as shown in Figure 12. When C = 0, the pyramid transforms into Coulomb-Mohr pyramid; when C = 0, A = -B, the pyramid degenerates into the Tresca hexagonal prism. If A = B = C, Equation (27) gives the trace of octahedral plane.

(2) Tsai-Wu Criterion[40]

$$A(\sigma_1 + \sigma_2 + \sigma_3) + B(\sigma_1^2 + \sigma_2^2 + \sigma_3^2) + C(\sigma_1\sigma_2 + \sigma_2\sigma_3 + \sigma_3\sigma_1)$$
$$= 1 \tag{28}$$

or

$$\sqrt{3}\, A\sigma_3^* + B(\sigma_1^{*2} + \sigma_2^{*2} + \sigma_3^*) - C\left[\frac{1}{2}(\sigma_1^{*2} + \sigma_2^{*2}) - \sigma_3^{*2}\right] = 1 \tag{29}$$

29

$\left\{ \dfrac{1}{A+B+C},\ \dfrac{1}{A+B+C},\ \dfrac{1}{A+B+C} \right\}$

LIMIT CONTOUR IN
π-PLANE PASSING
THROUGH ORIGIN

$A\sigma_i + B\sigma_j + C\sigma_k = 1$

σ_3

σ_2

σ_T

σ_1

$-\sigma_5$

$(0, -P, -P)$
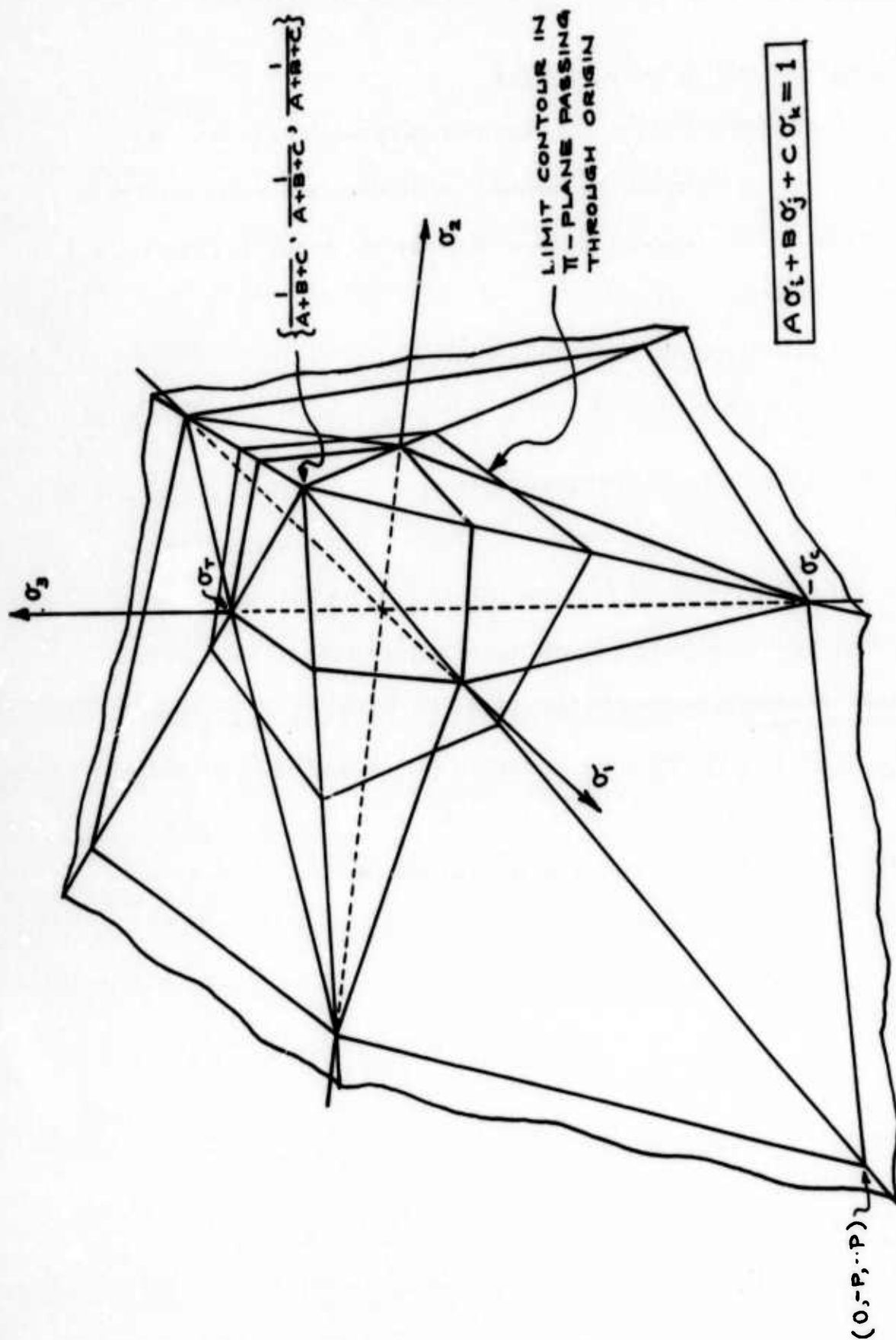
FIGURE 12.   HEXAGONAL PYRAMIDAL LIMIT SURFACE IN PRINCIPAL STRESS SPACE BASED
ON PAUL-HAYTHORNTHWAITE CRITERION (THREE-PARAMETRIC SURFACE)

30

This criterion is a linear combination of the mean normal stress and the normal stress quadratic terms. The associated limit surface is an ellipsoid of revolution, whose axis of revolution is the hydrostatic vector as shown in Figure 13. The two vertices are located on the space diagonal at $\sigma_3^* = \dfrac{-\sqrt{3}\, A \pm \sqrt{3 A^2 + 4(B + C)}}{2(B + C)}$, and the radius of a circular contour in a π-plane is $\left[\dfrac{2}{2B - C} \{1 - \sqrt{3}\, A\, \sigma_3^* - (B + C)\, \sigma_3^{*2}\}\right]^{\frac{1}{2}}$. Since the surface is ellipsoidal, the limit locus on a coordinate surface is an ellipse. In terms of σ_T, σ_C, and P (the magnitude of ultimate biaxial compressional stress), A, B, and C have the forms

$$A = \frac{\sigma_C - \sigma_T}{\sigma_T \sigma_C} \tag{30}$$

$$B = \frac{1}{\sigma_T \sigma_C} \tag{31}$$

$$C = \frac{1}{P^2}\left[1 + \frac{2P}{\sigma_T \sigma_C}\,(\sigma_C - \sigma_T - P)\right] \tag{32}$$

When $\sigma_C \longrightarrow \infty$, $P \longrightarrow \infty$, we have $A \longrightarrow \dfrac{1}{\sigma_T}$, $B \longrightarrow 0$, $C \longrightarrow 0$, and Equation (28) becomes

$$\sigma_1 + \sigma_2 + \sigma_3 = \sigma_T \tag{33}$$

and the ellipsoidal surface degenerates to the principal octahedral plane. If $A = 0$, and $B = -C$, the ellipsoid will transform into the Mises cylinder.

31
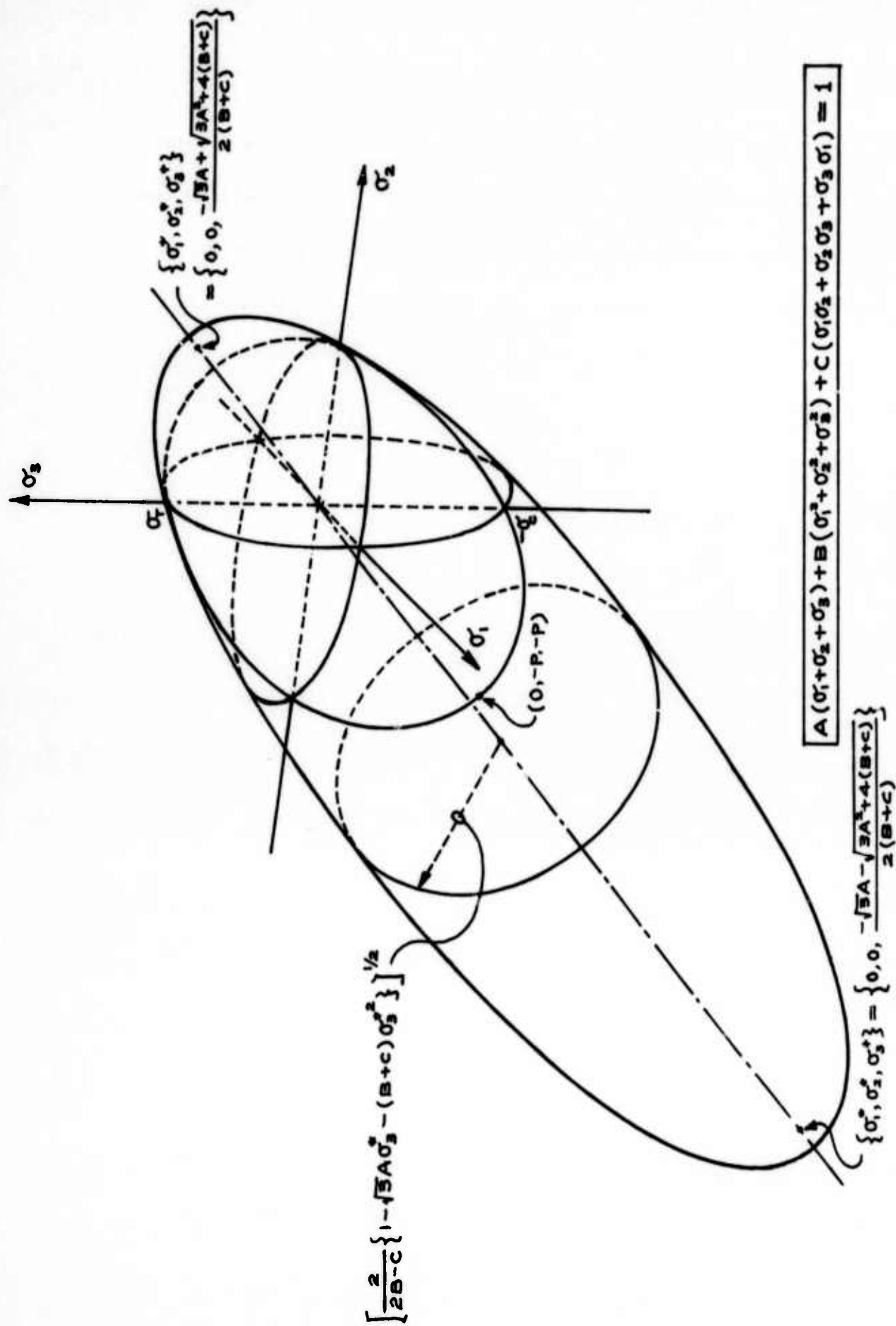
FIGURE 13. ELLIPSOID-OF-REVOLUTION LIMIT SURFACE IN PRINCIPAL STRESS SPACE BASED ON TSAI-WU CRITERION (THREE-PARAMETRIC SURFACE)

$$A(\sigma_1 + \sigma_2 + \sigma_3) + B(\sigma_1^2 + \sigma_2^2 + \sigma_3^2) + C(\sigma_1\sigma_2 + \sigma_2\sigma_3 + \sigma_3\sigma_1) = 1$$

$$\{\sigma_1^*, \sigma_2^*, \sigma_3^*\} = \left\{0, 0, \frac{-\sqrt{3}A + \sqrt{3A^2 + 4(B+c)}}{2(B+c)}\right\}$$

$$\{\sigma_1^*, \sigma_2^*, \sigma_3^*\} = \left\{0, 0, \frac{-\sqrt{3}A - \sqrt{3A^2 + 4(B+c)}}{2(B+c)}\right\}$$

$$\left[\frac{2}{2B-c}\left\{1 - \sqrt{3}A\sigma_3^* - (B+c)\sigma_3^{*2}\right\}\right]^{1/2}$$

$(0, -P, -P)$

32

(3)   Priddy Criterion[28]

$$A I + B II_D + C III_D = 1 \tag{34}$$

or

$$\sqrt{3}\, A \sigma_3^* + \frac{3}{2} B\, (\sigma_1^{*2} + \sigma_2^{*2}) + \frac{3\sqrt{6}}{2} C \sigma_2^* (3\sigma_1^{*2} - \sigma_2^{*2}) = 1 \tag{35}$$

This criterion is a linear combination of the mean normal stress and the second and third deviatoric stress invariants. Inclusion of the I term causes the limit surface to vary along the space diagonal, while inclusion of the III_D term, as discussed earlier, distorts the Mises circle into a trigonally symmetric shape. The limit surface given by Equation (34) is the tri-saddled cubic surface shown in Figure 14. In the region $0 \leq r \leq r_s$, where r is a radial distance from the space diagonal and r_s is the radial coordinate for the three saddle points located in trigonally symmetric fashion, the central portion of the limit surface is bell shaped, with its vertex located on the space diagonal at $\sigma_3^* = \frac{1}{\sqrt{3}\,A}$ (or $\sigma_1 = \sigma_2 = \sigma_3 = \frac{1}{3A}$). The contour of this bell-shaped surface forms a three-lobed figure which varies along the space diagonal. When $r > r_s$ (i.e., beyond the saddle points), the three outermost regions of the bell-shaped surface then open up to form three curved open channels. The upper portions ($\sigma_3^* > \sigma_{3s}^*$, where σ_{3s}^* refers to the location of the saddle points) of the channels are cat-ear-shaped, with tips lying in the π-plane passing through the vertex of the bell-shaped portion. The lower portions ($\sigma_3^* < \sigma_{3s}^*$) of the channels
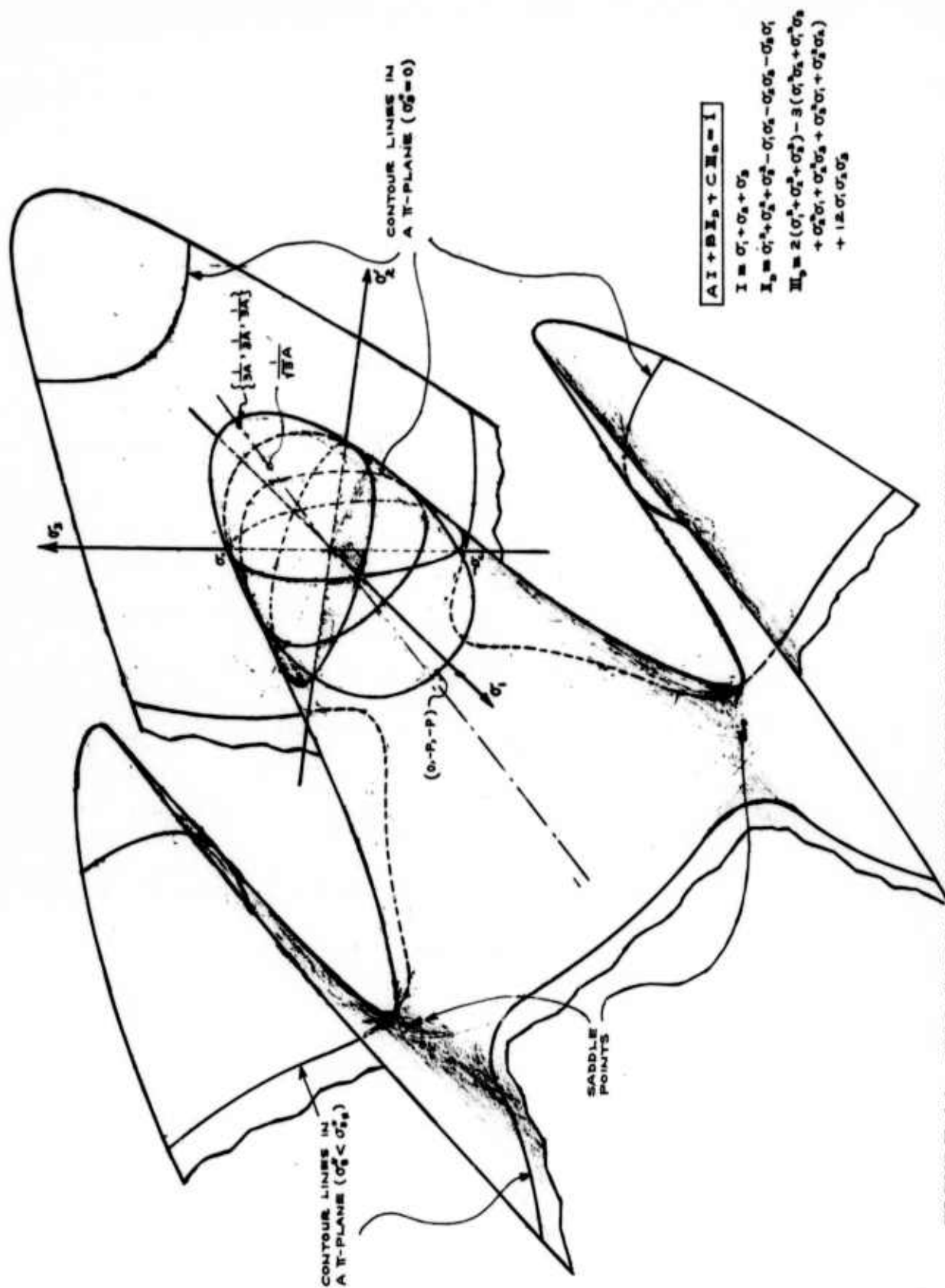
33

FIGURE 14. TRI-SADDLED CUBIC LIMIT SURFACE BASED ON PRIDDY CRITERION
(THREE-PARAMETRIC SURFACE)

34

are bottomless. In application of Equation (34) to actual materials, these curved channels are "non-physical," and should be disregarded. Contour lines of the entire limit surface in two π-planes (i.e., $\sigma_3^* = 0$, $\sigma_3^* < \sigma_{3s}^*$) and limit loci are also shown in the figure.

The three strength constants A, B and C, when related to σ_T, σ_C, and P, have the following forms.

$$A = \frac{P^2 (\sigma_T^2 - \sigma_T\sigma_C + \sigma_C^2) - P^3 (\sigma_T - \sigma_C) - \sigma_T^2\sigma_C^2}{\sigma_T\sigma_C P \left[P^2 - P(\sigma_T - \sigma_C) + 2\sigma_T\sigma_C \right]} \tag{36}$$

$$B = \frac{P^3 + 2P (\sigma_T^2 - \sigma_T\sigma_C + \sigma_C^2) - \sigma_T\sigma_C (\sigma_T - \sigma_C)}{\sigma_T\sigma_C P \left[P^2 - P(\sigma_T - \sigma_C) + 2\sigma_T\sigma_C \right]} \tag{37}$$

$$C = -\frac{P^2 + 2P (\sigma_T - \sigma_C) - \sigma_T\sigma_C}{2\sigma_T\sigma_C P \left[P^2 - P(\sigma_T - \sigma_C) + 2\sigma_T\sigma_C \right]} \tag{38}$$

When $A \longrightarrow 0$, the saddle points will recede to negative infinity in the (---) octant, while the apex of the bell-shaped portion and the tips of the channels will move to positive infinity in the (+++) octant, transforming the Priddy limit surface to the Sobotka limit surface shown in Figure 11.

(4) Mogi Criterion[41]

$$AI + BII_D + C\sigma_2 = 1^* \quad ; \quad i = 1, 2, 3 \tag{39}$$

---

* The original form given by Mogi is $\tau_{oct} = f (I - (1 - \alpha)\sigma_i)$, where τ_{oct} is the octahedral shearing stress, and α is a constant less than unity.

This criterion postulates that the distortional energy at failure depends linearly on the mean normal stress and the intermediate principal stress. The limit surface associated with this criterion is shown in Figure 15. Due to inclusion of the σ_i term in the criterion, the Torre paraboloid of revolution (see Figure 8) is deformed into a composite paraboloidal limit surface which is generated by fusing together portions of three identical paraboloids of revolution. The resultant surface is trigonally symmetric, with axes parallel to the space diagonal, and located at a distance $\frac{\sqrt{6}\,C}{9\,B}$ from the space diagonal. The contour line of the limit surface in the π-plane is then a three-lobed figure, each lobe of which is a circular arc of radius $\left[\frac{2}{3\,B}\left\{1 - \sqrt{3}\,(A + \frac{C}{3})\,\sigma_3{}^* + \frac{C^2}{9\,B}\right\}\right]^{\frac{1}{2}}$. The apex of this limit surface is located on the space diagonal at $\sigma_3{}^* = \frac{\sqrt{3}}{3\,A + C}$ (or $\sigma_1 = \sigma_2 = \sigma_3 = \frac{1}{3\,A + C}$).

In terms of σ_T, σ_C, P, the three strength constants A, B, C in Equation (39) can be expressed as

$$A = \frac{P^2 - \sigma_C{}^2}{\sigma_C\,P\,(2\,\sigma_C - P)} \tag{40}$$

$$B = \frac{2P - \sigma_C}{\sigma_C\,P\,(2\,\sigma_C - P)} \tag{41}$$

$$C = \frac{\left[\sigma_T\sigma_C - 2\,P\,(\sigma_T - \sigma_C) - P^2\right](\sigma_T + \sigma_C)}{\sigma_T\sigma_C\,P\,(2\,\sigma_C - P)} \tag{42}$$
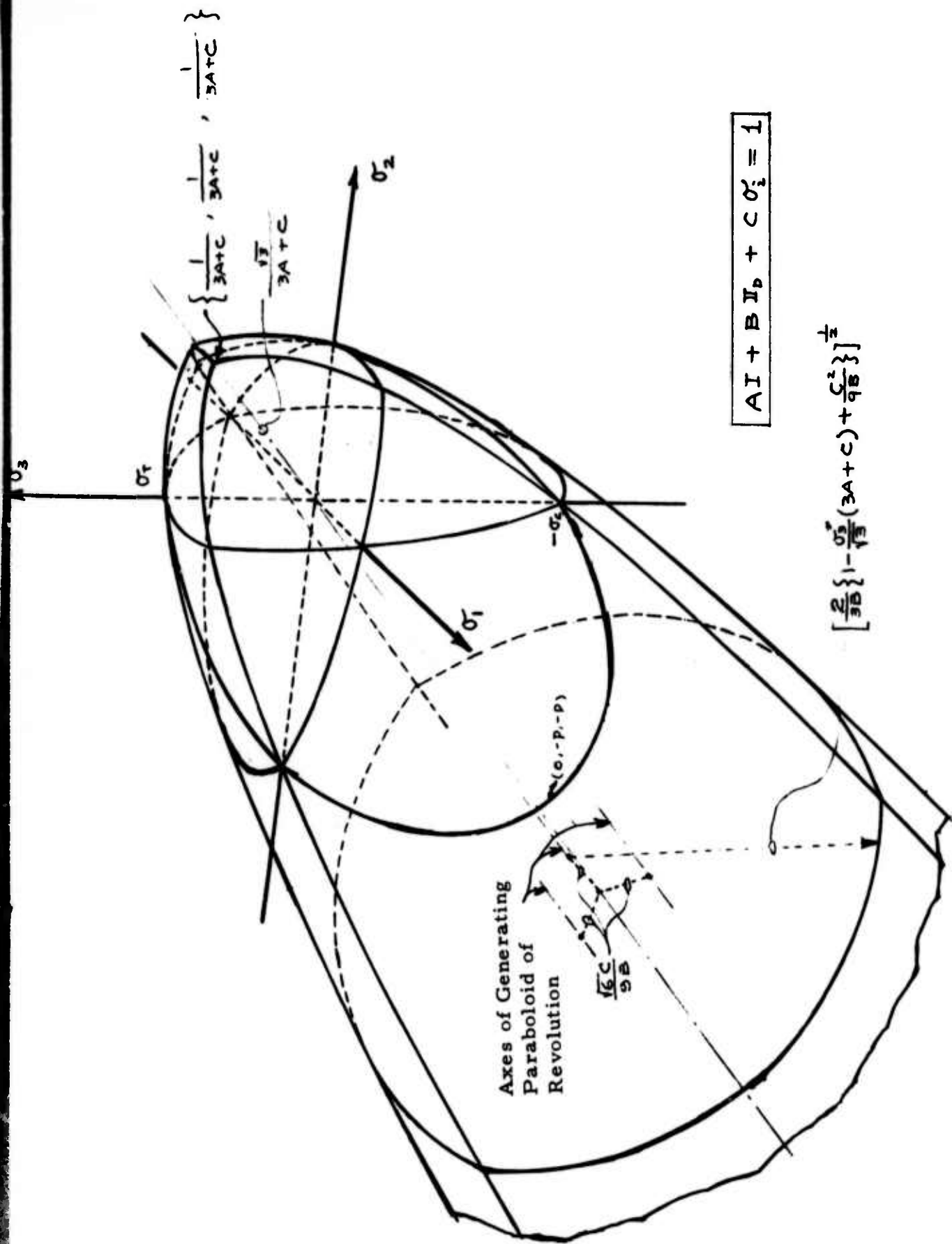
FIGURE 15. TRI-PARABOLOIDAL LIMIT SURFACE IN PRINCIPAL STRESS SPACE
BASED ON MOGI CRITERION (THREE-PARAMETRIC SURFACE)

$$\boxed{A I + B I_b + C \sigma_i^2 = 1}$$

$$\left[\frac{2}{3B}\left\{1 - \frac{\sigma_3}{\sqrt{3}}(3A+C) + \frac{C^2}{9B}\right\}\right]^{\frac{1}{2}}$$

37

Four-Parametric Limit Surface

By increasing the number of terms (i.e., the number of adjustable strength constants) in Equation (1) it is possible to improve the fitting of a limit surface to the failure data; however, the functional simplicity of the failure criterion can be lost. As mentioned earlier, if the cubic term is introduced, one can distort the Mises circle (arising from the term II_D) into a three-fold symmetric continuous contour, but undesirable portions in the resulting limit surface always result. In order to avoid the cubic and higher order terms, and yet provide the failure criterion with four terms and the capability of generating a limit surface with a trigonally symmetric contour line in the π-plane, one can formulate the following four parametric limit surface equations,

$$AI + B II_D + C \sigma_i + D \sigma_j = 1^* \quad ; \quad i, j = 1, 2, 3 \tag{43}$$

where A, B, C, and D are the four adjustable strength constants.

The limit surface given by Equation (43), and shown in Figure 16, is a hexa-paraboloidal shape consisting of six segments of identical paraboloids of revolution whose axes are parallel to the space diagonal and located at a distant $\frac{\sqrt{2}}{3 \sqrt{3} \, B} \sqrt{C^2 - CD + D^2}$ from the diagonal in trigonal symmetry. The apex of the limit surface is located on the space diagonal at $\sigma_3^* = \frac{\sqrt{3}}{3A + C + D}$ (or $\sigma_1 = \sigma_2 = \sigma_3 = \frac{1}{3A + C + D}$). The associated

---

$^*AI + C\sigma_i + D\sigma_j = 1$ may be identified as Paul-Haythornthwaite criterion.

FIGURE 16.   HEXA-PARABOLOIDAL LIMIT SURFACE IN PRINCIPAL STRESS SPACE
BASED ON A FOUR-PARAMETRIC FAILURE CRITERION

contour line in a π-plane is then made up of six circular arcs of the same radius $\left[\dfrac{2}{3\,B}\left\{1 - \dfrac{\sigma_3^*}{\sqrt{3}}(3\,A + C + D) + \dfrac{1}{9\,B}(C^2 - CD + D^2)\right\}\right]^{\frac{1}{2}}$.

The four strength constants A, B, C and D, when related to σ_T, σ_C, P and S (magnitude of ultimate normal stress inducing pure shear), have the following forms

$$A = \frac{S\,(\sigma_T + \sigma_C)\left[P^2 + P\,(\sigma_T - \sigma_C) - \sigma_T\sigma_C\right] + \sigma_T\,(\sigma_C - P)\,(\sigma_C P + 3\,S^2)}{\sigma_T\sigma_C\,P\,S\,(\sigma_T + \sigma_C - 3\,S)} \tag{44}$$

$$B = \frac{S\,(\sigma_T + \sigma_C) - \sigma_T\sigma_C}{\sigma_T\sigma_C\,P\,S\,(\sigma_T + \sigma_C - 3\,S)} \tag{45}$$

$$C = \left\{S(\sigma_T + \sigma_C)\left[\sigma_T\sigma_C - 2\,P\,(\sigma_T - \sigma_C) - P^2\right] + \sigma_T\sigma_C\,(P^2 - 3\,S^2)\right.$$
$$\left. + P\,(\sigma_T - \sigma_C)\,(\sigma_T\sigma_C + 3\,S^2)\right\} \Big/ \left[\sigma_T\sigma_C\,P\,S\,(\sigma_T + \sigma_C - 3\,S)\right] \tag{46}$$

$$D = \left\{S\,(\sigma_T + \sigma_C)\left[\sigma_T\sigma_C - 2\,P\,(\sigma_T - \sigma_C) - P^2\right] + \sigma_T\sigma_C\,(P^2 - 3\,S^2)\right.$$
$$\left. - 2\,\sigma_T\,P\,(\sigma_C^2 - 3\,S^2)\right\} \Big/ \left\{\sigma_T\sigma_C\,P\,S\,(\sigma_T + \sigma_C - 3\,S)\right\} \tag{47}$$

It can be seen that the four parametric failure criterion given by Equation (43) contains the Tresca, Mises, Coulomb-Mohr, Torre, Paul-Haythornthwaite and Mogi criteria as special cases.

EXPERIMENTAL RESULTS

Uniaxial Compression Tests

The most simple manner in which to consider the deformation data
is in terms of the stress-strain curve. Figure 17, for example, shows
both the stress-longitudinal strain (ϵ_x) and the stress-circumferential
strain (ϵ_θ) relationships for a specimen tested at room temperature.
Each curve has two fairly well-defined points of inflection. In particular,
the curves deviate from linear elastic behavior (Stage I) at around 20 KSI
and become somewhat more dramatically nonlinear in the vicinity of 50 KSI.
Failure in this particular specimen occurred at 63 KSI. The nonlinear
regions may be realized more clearly when plotted on a log-log basis in
terms of plastic strains. The stress-longitudinal plastic strain relation-
ship is represented thusly in Figure 18, in which the two stage nonlinear
relation is given by $\sigma \propto \epsilon_p^{-2.5}$ during the first (Stage II region and by $\sigma \propto \epsilon_p^{-4}$
during the second (Stage III). At lower temperatures similar behavior is
observed, the principal difference being that the transition to Stage III
occurs at a much higher stress level, as does the failure stress.[1]

The same data behave as shown in Figure 19 if the strains are re-
cast in the form of relative volume change $\Delta V/V_0$, defined as $\epsilon_x + 2 \epsilon_\theta$.
Again, there is an inflection (amounting to volumetric dilatancy) away from
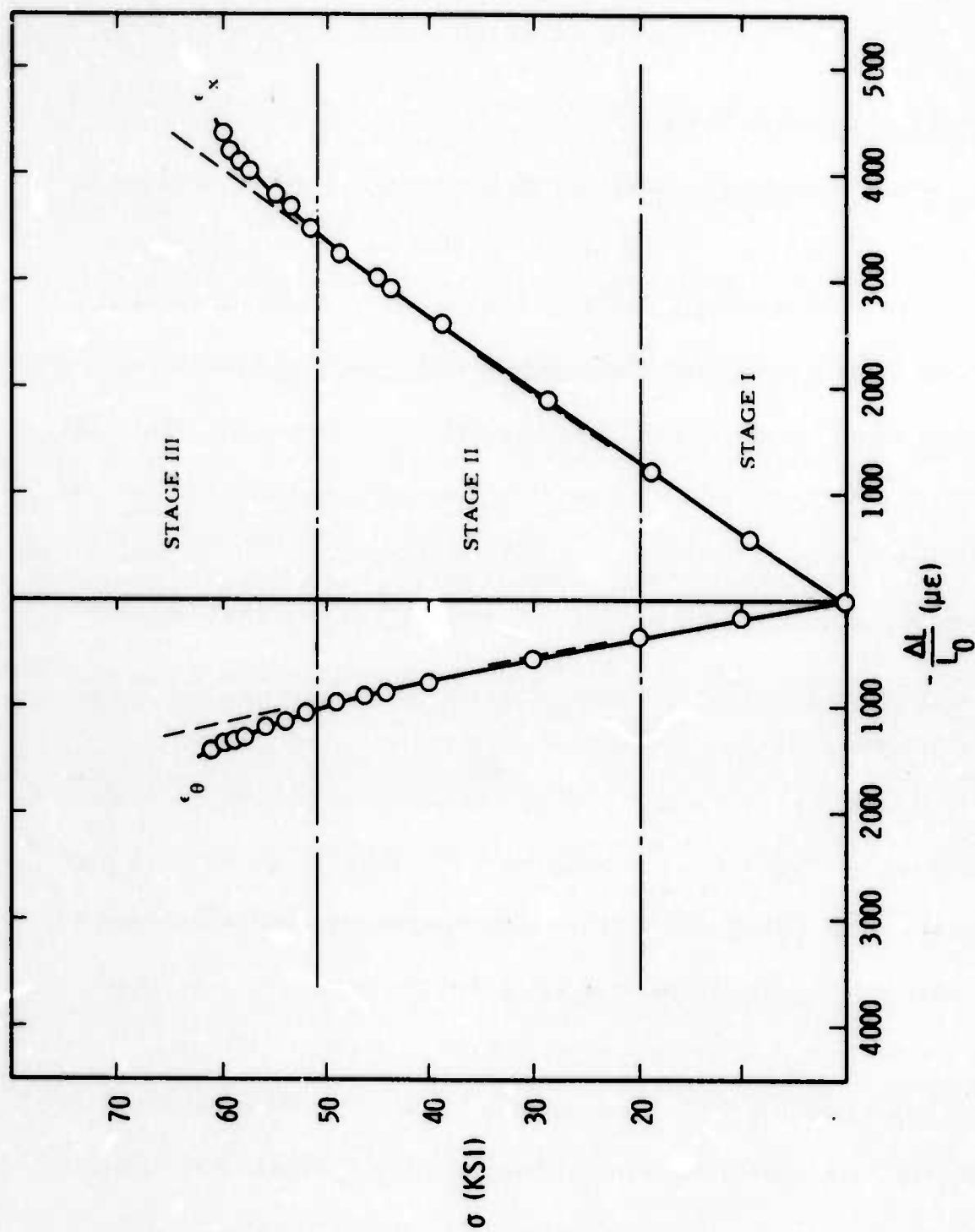linear elasticity at a stress level of approximately 20 KSI. The room

41

FIGURE 17. PLOT OF STRESS VS BOTH AXIAL AND
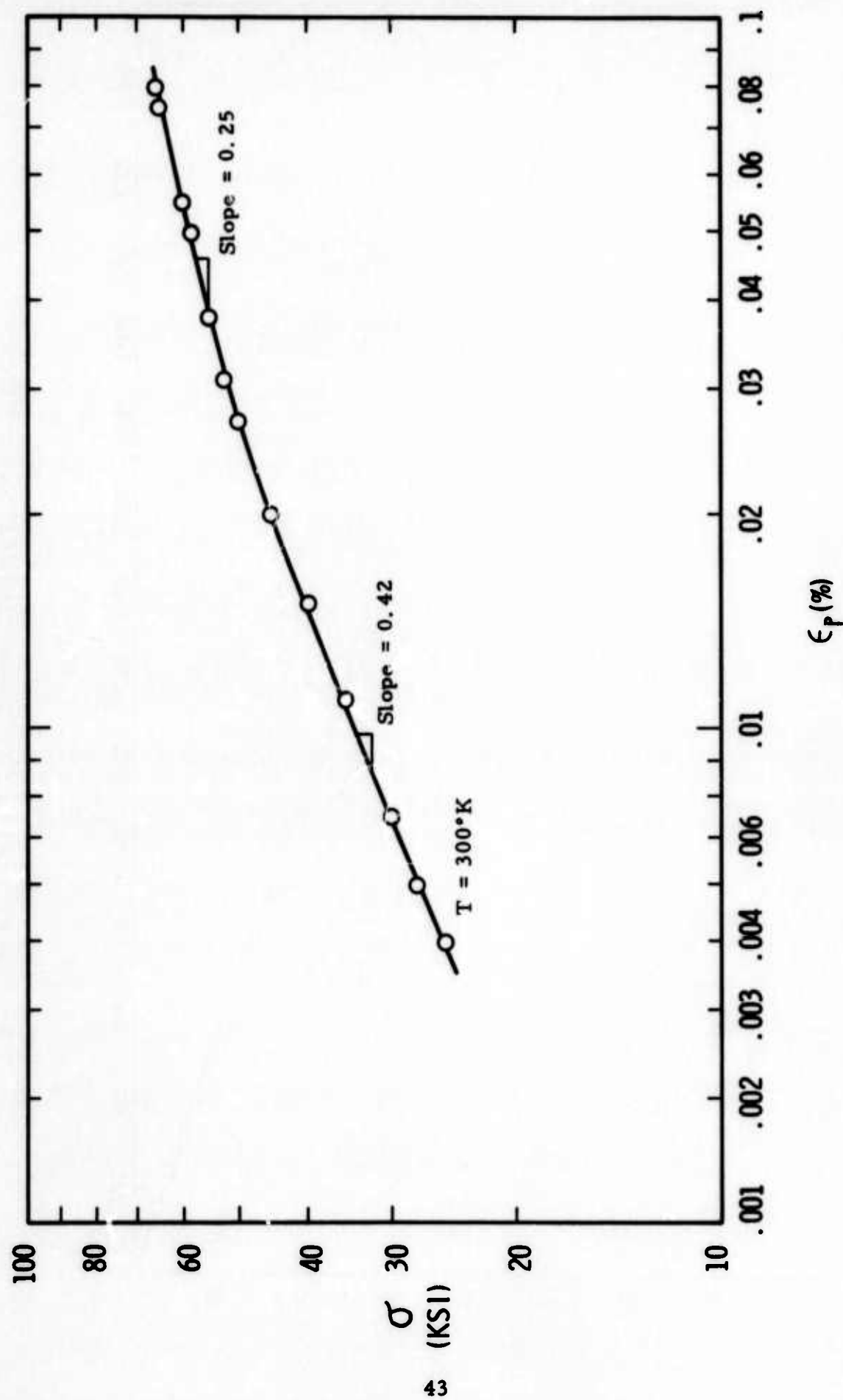CIRCUMFERENTIAL STRAIN

42
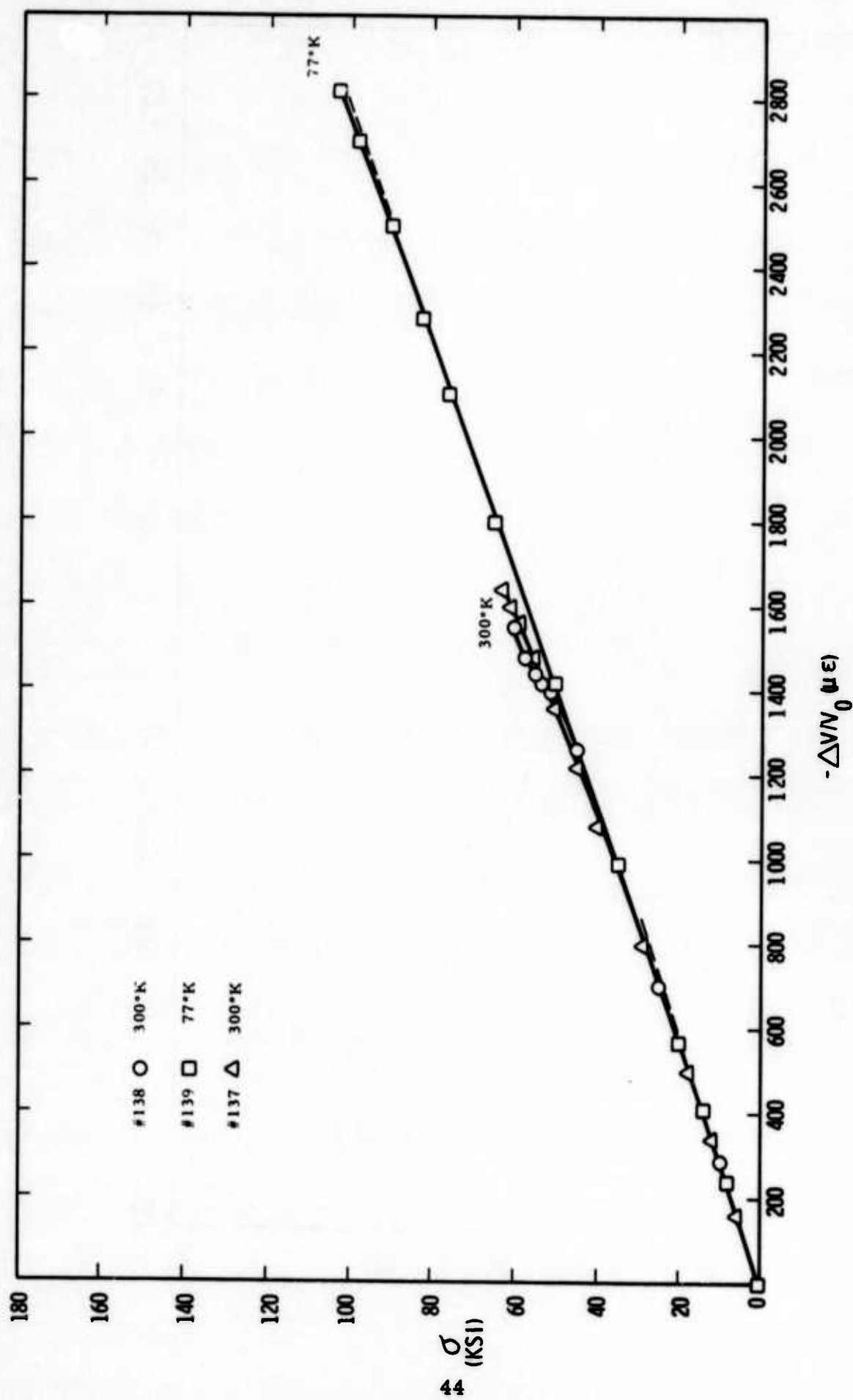
FIGURE 18. PLOT OF STRESS VS PLASTIC STRAIN

FIGURE 19. EFFECT OF TEMPERATURE ON DILATANCY

44

temperature plots are nearly linear thereafter until the onset of more
macroscopic dilatancy prior to fracture. No significant dilatancy is ob-
served at 77°K. It should be recalled that the circumferential strain
gages used in these experiments are too small to respond to the gross
dilatancy corresponding to fault formation during failure, so that actual
net volume increases are not recorded.

A useful, alternate method of presenting the dilatancy is to plot
stress as a function of volume change for successive cyclic stress ampli-
tudes. Such data for a 300°K test are shown in Figure 20. It is interest-
ing to note that at a stress level of 20 KSI, some slight hysteresis in the σ
vs $\Delta V/V_0$ loop is apparent. The maximum loop opening in this case is of
the order of only 10 microstrains. Essentially no loop opening exists at
lower stresses. As successively higher stress cycles are run, the amount
of hysteresis increases, as shown by the 30 KSI loop. The same qualita-
tive behavior was observed at 77°K as well. On the basis of the hysteresis
loop data, it now appears that the "elastic limit" is much lower than appeared
to be the case during the course of the preceding work,[1] in which the limit
was estimated from the apparent deviation from linearity of the macroscopic
(low strain sensitivity) stress-strain curve.

In Figure 21, some of the results obtained during the hysteresis
energy loss experiments are shown. It will be recalled that ΔE is defined
simply as the closed area within a hysteresis loop, i.e., $\Delta E = \oint \sigma \, d\epsilon$, and
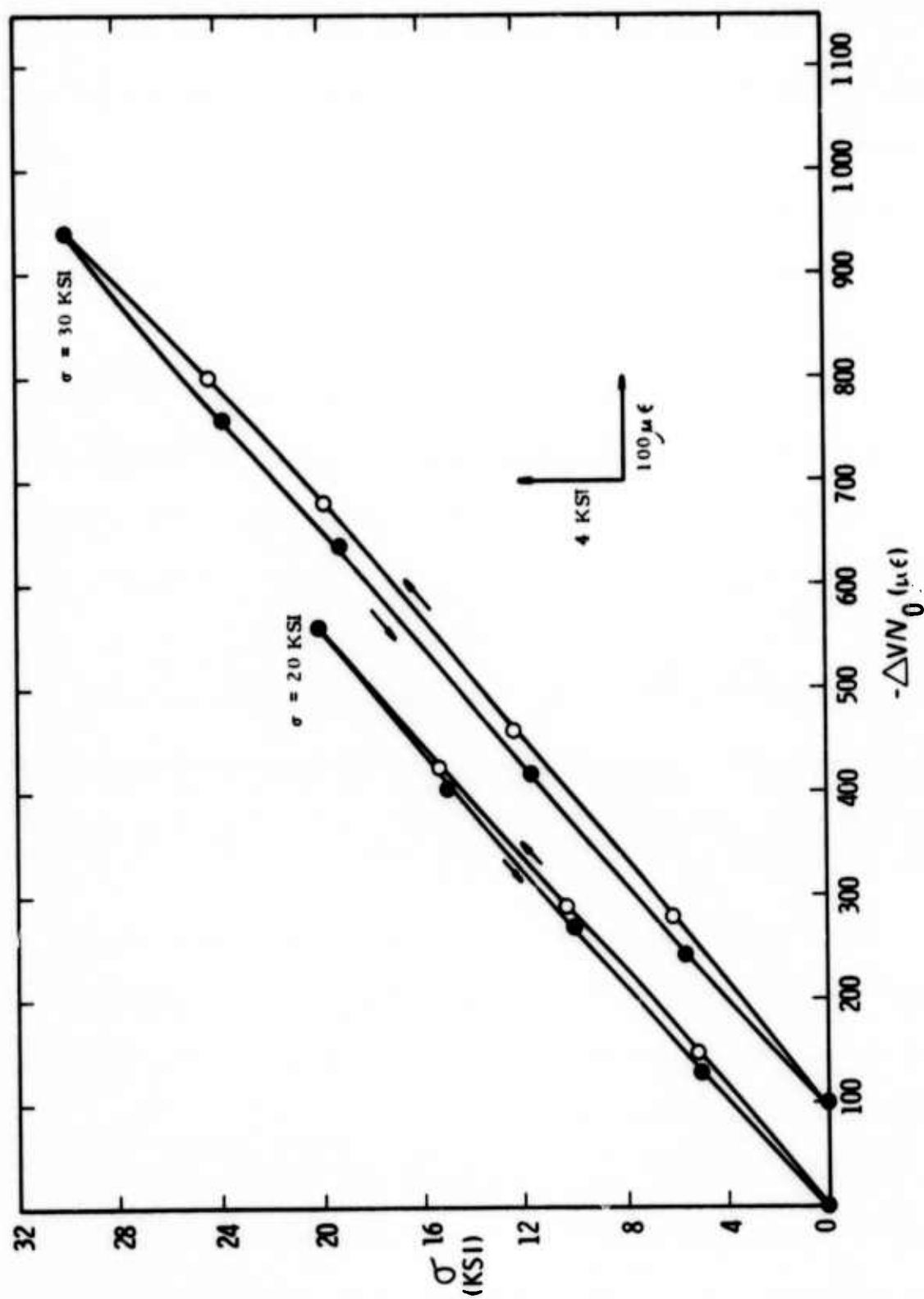
FIGURE 20. REPRESENTATIVE STRESS-VOLUMETRIC STRAIN HYSTERESIS LOOPS
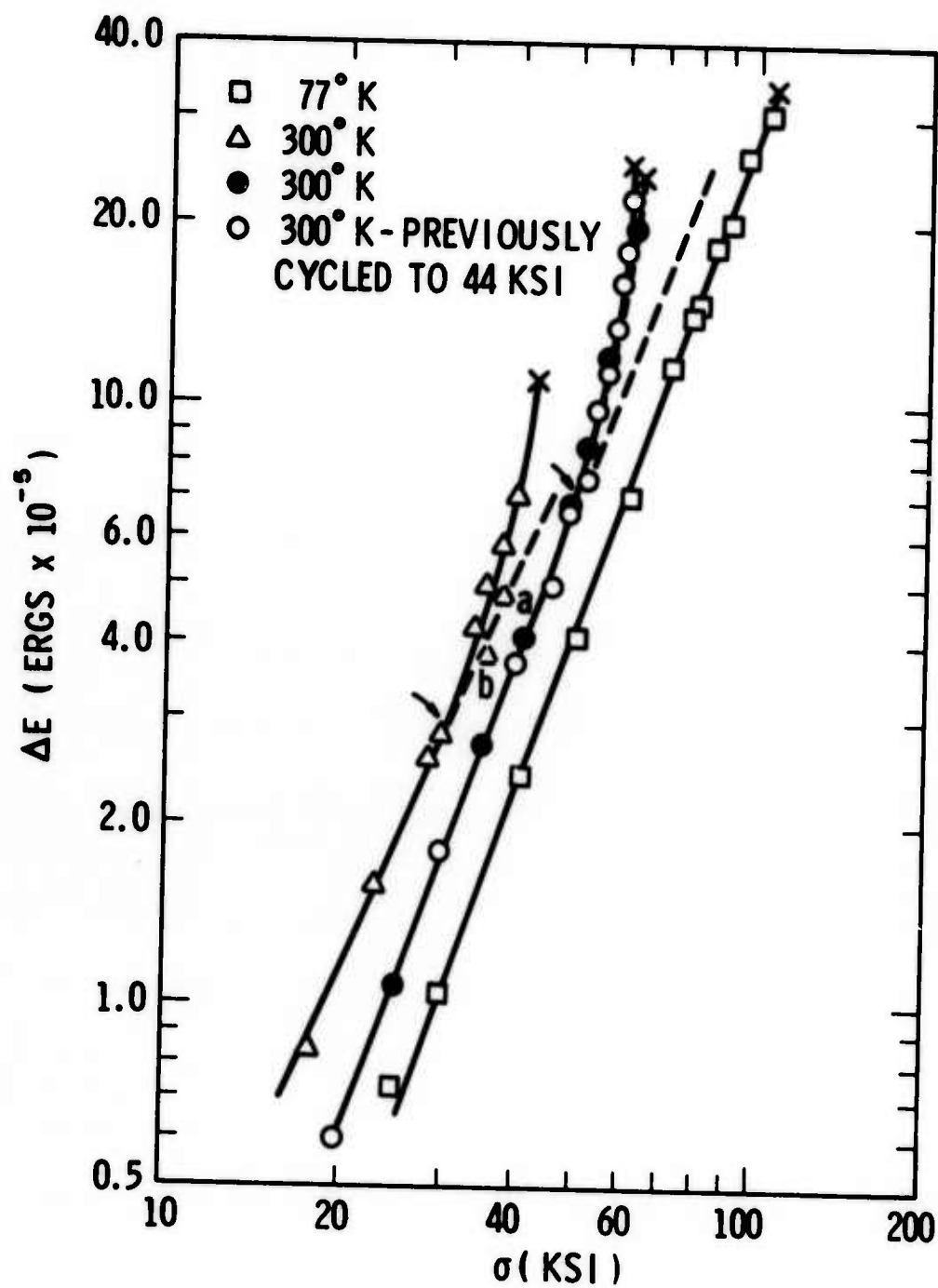
46

FIGURE 21.   HYSTERESIS ENERGY LOSS VS
STRESS AMPLITUDE

47

is a measure of the irreversible energy lost during a single stress cycle. Interestingly, the initial slope $(\frac{\Delta E}{\sigma})$ for all tests run thus far seemed relatively independent of both ultimate strength and temperature. In fact, if we write $\Delta E \propto \sigma^n$, it is found that $2.4 \leq n \leq 2.64$. This initial, minimum slope is maintained almost to failure for the low temperature ($77^\circ K$) tests. Room temperature behavior, however, is markedly different. In particular, at around 80% of the failure stress, there occurs a sudden increase in the "rate" of energy loss, which accelerates as failure is approached. It is instructive to note that the data plotted represent the energy lost during the very first cycle at each successively higher stress level. Subsequent loops at the same level always were of equal area for stresses below the inflection point, but once the acceleration in energy loss began, all loops after the first were smaller than the first loop. Two data points representing the second loops run at the indicated stresses are shown in Figure 21 by letters (a and b). Not only are the loop areas smaller than those obtained during the initial cycles, but the measured energy losses lie very near the values one would have expected on the basis of extrapolation of the linear region below the inflection point.

## Microcrack Initiation and Growth

The general sequence of microfracturing events preceding ultimate failure was established by means of the replication technique. The nature of the initiation event was examined in greater detail by "backtracking"

through the replicas, defining the initiation site, and then turning to the actual, unfailed specimen for closer study in the SEM.
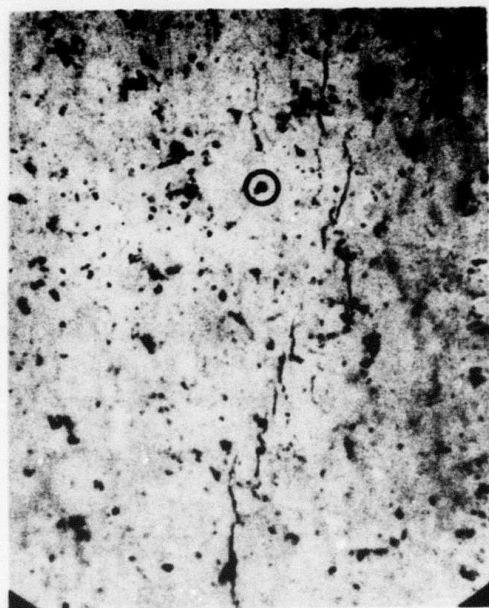
Development of several microcrack networks within a single specimen will be presented, in order to establish the usual pattern of development. In some of the sequences, a landmark feature has been circled so that equivalent locations can be located quickly in sequential photomicrographs. In all cases, the compressive stress axis is vertical, and arrows indicate initiation sites. The stresses refer to the level of compressive loading to which the specimen was subjected prior to replication of the surface flat.

The first sequence (Fig. 22) shows a set of en echelon, axially oriented microcracks which apparently initiated between 34 and 36 KSI. At 36 KSI the cracks (arrows) can barely be resolved, while they are readily apparent at 38 KSI. The ΔE-σ curve for this specimen is plotted in Figure 23, from which it can be seen that the first cracks were formed after the inflection point in the curve; the sketch (A) indicates the relative state of total microcrack development on the surface flat at this point. It should be emphasized that the set of cracks shown in the photomicrograph sequence corresponds to just one of the dot-like segments in the sketch.

A different sort of sequence can be seen in Figure 24. Here the first vestige of a microcrack was detected (arrow) at 28 KSI. This is somewhat below the inflection point, but again the initial position of the cracks

49
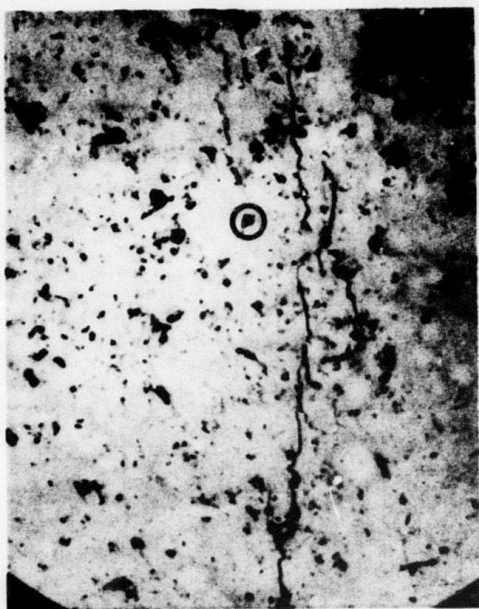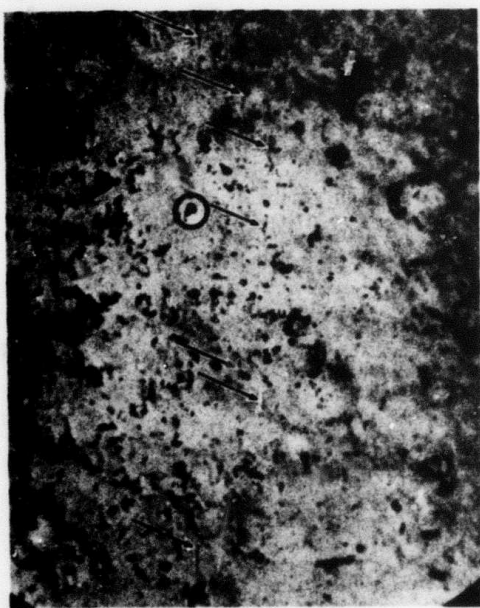
(a) 40 KSI
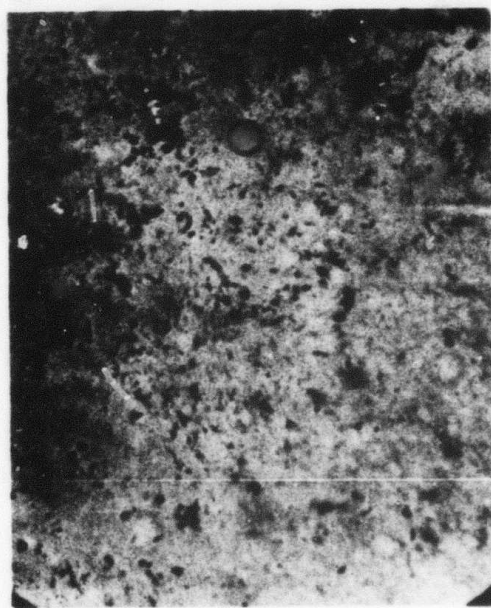
(b) 38 KSI

(c) 36 KSI

(d) 34 KSI

FIGURE 22.   DEVELOPMENT OF MICROCRACK NETWORK.
CIRCLE INDICATES REFERENCE LANDMARK (250x)

FIGURE 23. HYSTERESIS ENERGY LOSS VS STRESS AMPLITUDE
FOR A REPLICA SPECIMEN, SHOWING
SEQUENTIAL MICROFRACTURING

(a) 40 KSI

(b) 38 KSI

(c) 36 KSI

(d) 34 KSI

FIGURE 24. DEVELOPMENT OF MICROCRACK NETWORK.
CIRCLE INDICATES REFERENCE LANDMARK (250x)

(e) 32 KSI

(f) 30 KSI

(g) 28 KSI

(h) 26 KSI

FIGURE 24 (CONTINUED)

53

is en echelon. However, crack development within this region is fairly complete at a stress level of 34 KSI, in contrast to the first case. Again, the general state of crack development at the time of initiation of this partic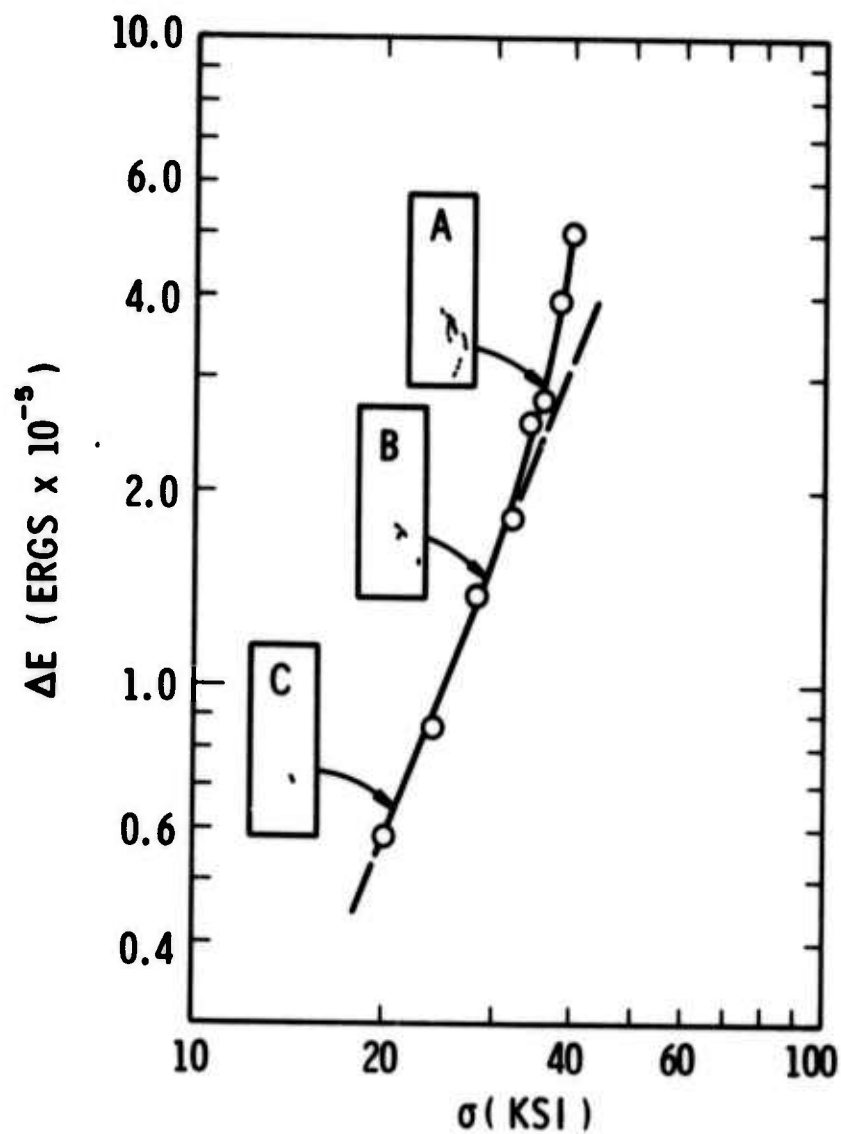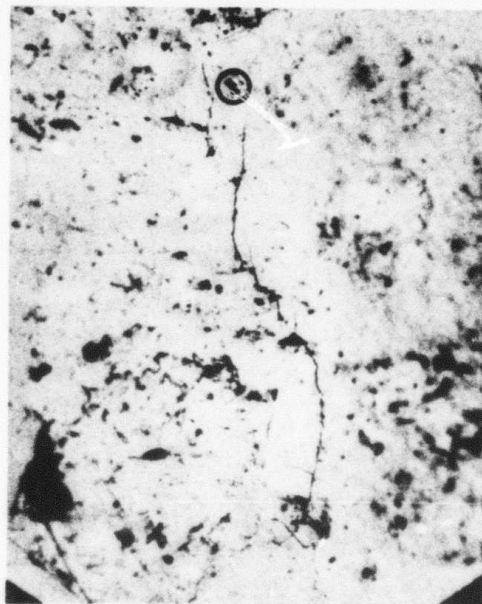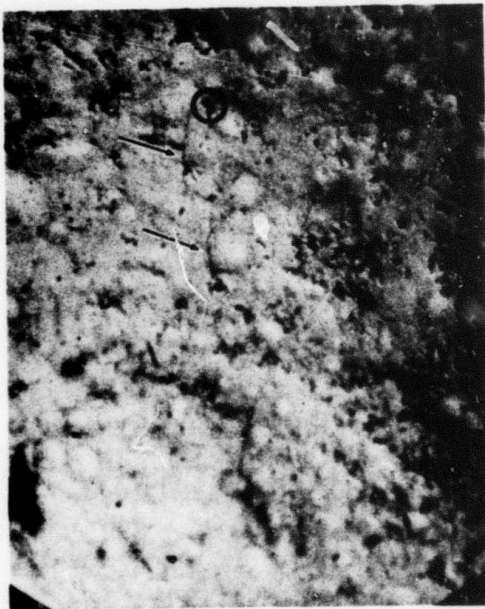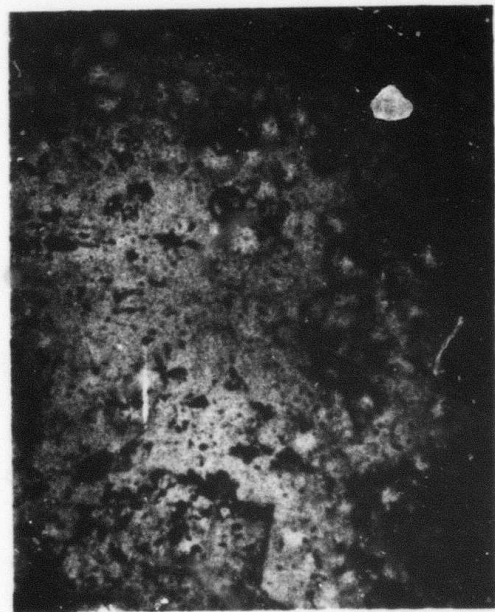ular network is shown in (B) of Figure 22. By looking at this region of the actual rock specimen under high magnification in the SEM (Fig. 25), the generally intragranular character of the crack manifests itself. Two basic mineral constituents predominate, one light, one darker. Grain boundary resolution in this case is caused not by surface relief, or grain boundary cracking, as can be easily verified from Figure 26, a Nomarski phase contrast optical photomicrograph of the same region. The grain boundaries previously visible in the SEM are indiscernible. It is interesting to note that the two crack initiation sites (arrows) shown in Figure 24 correspond to the two light-colored regions (arrows) in Figure 25. We shall return to this point later.

An almost classic example of en echelon, axially-oriented cracking is provided by the sequence of Figure 27. Note in particular the crack array of Figure 27c. An SEM magnified view of the crack initiation site is provided by Figure 28, in which the first crack is observed to lie in the dark mineral constituent. In general, it was found that crack initiation could occur in either the light or the dark phase, but that initiation, as well as subsequent propagation, was essentially transgranular. Generally, grain boundary pores and minor constituent phases (grains) were associated with

FIGURE 25.   HIGH MAGNIFICATION (600x) PHOTO, USING SEM,
OF REGION SHOWN IN FIGURE 24

FIGURE 26. HIGH MAGNIFICATION (600x) PHOTO, USING
NOMARSKI CONTRAST, OF REGION SHOWN
IN FIGURE 24

56
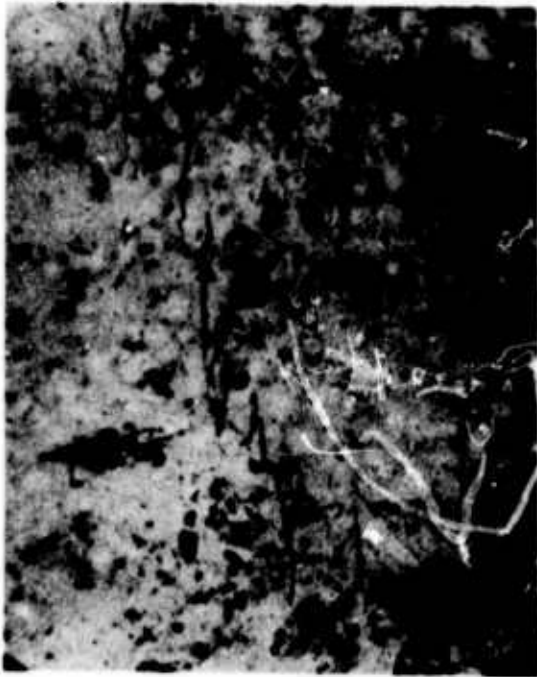
(a) 40 KSI
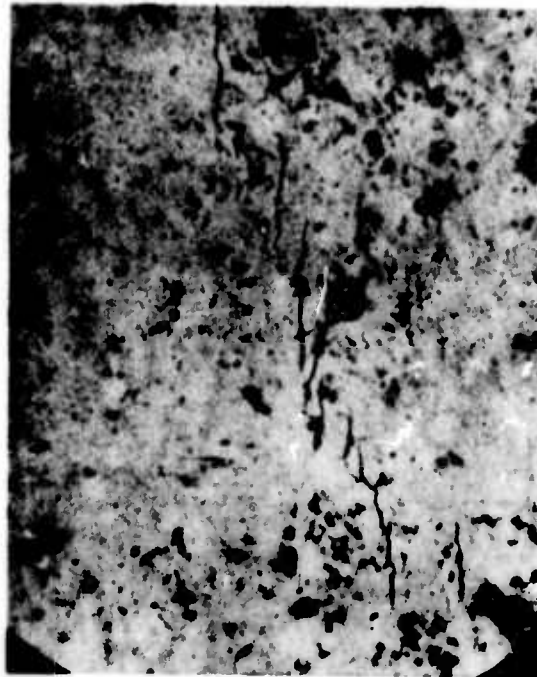
(b) 38 KSI
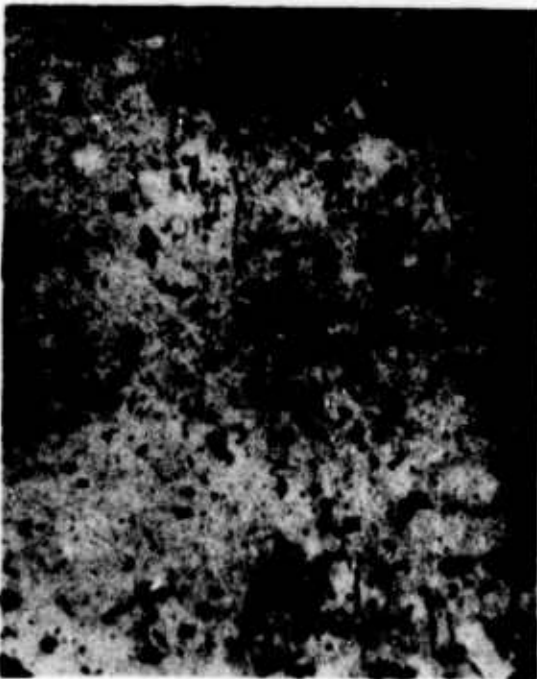
(c) 36 KSI

(d) 34 KSI

FIGURE 27.   DEVELOPMENT OF MICROCRACK NETWORK.
CIRCLE INDICATES REFERENCE LANDMARK (250X)

57

FIGURE 28.   600x SEM PHOTOMICROGRAPH OF
            CRACK INITIATION SITE IN
            FIGURE 27

initiation, but only as stress raisers. The cracks themselves usually did not follow pre-existing cracks or grain boundaries, and in fact, grain boundaries sometimes served as crack arrestors ("a" in Fig. 25).

The two primary mineral constituents of Dresser basalt, as previously mentioned, are plagioclase feldspar and pyroxene. From SEM spectroscopic analysis, it was determined that the light-colored regions contained Ca, Al, Fe, Mg, and Si, and hence seemed to constitute the pyroxene, while the Al, Na, and Si bearing dark regions apparently are feldspar. As an example, an SEM representation of elemental distribution is shown in Figure 29 for the crack initiation site of Figure 28. The elements selected were Mg, Na, Ca, and Fe. The distributions relate one-to-one with the photomicrograph of Figure 28, i.e., they may be overlaid. This is especially evident in terms of the calcium distribution, which rather clearly delineates the feldspar (dark) from the pyroxene (light).

The earliest crack development was detected, using replicas, at a stress level of 20 KSI. The location of this crack is shown in Figure 23(c); the crack was only 20 μm in length, and like most of the cracks which ultimately would extend in length, was oriented in an axial direction. Shear cracks were often observed, and in fact there were many cracks oriented almost perpendicular to the stress axis, but these usually were associated with previously nucleated axial cracks, and seemed to form in order to relax the stresses around the tips of the axial cracks. No evidence of dislocation type deformation (slip bands, slip lines) was ever detected, even
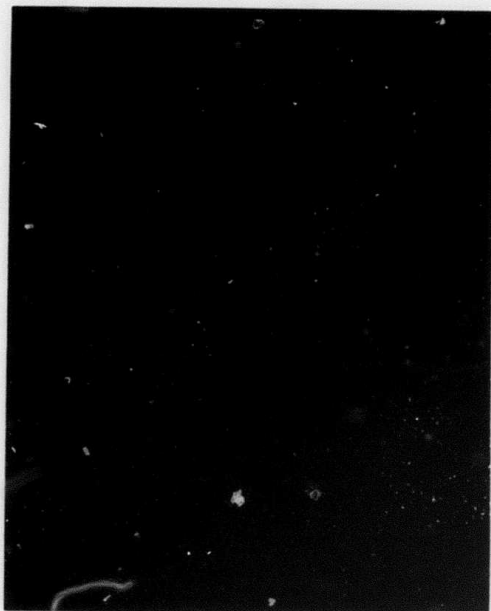
(a) Magnesium

(b) Sodium

(c) Calcium

(d) Iron

FIGURE 29.   ELEMENTAL DISTRIBUTION IN PHOTO-
MICROGRAPH OF FIGURE 28 (600x)

at the highest magnifications (2000 - 3000x) used. Cracks which nucleated at an angle of greater than $\sim 20^\circ$ relative to the stress axis almost never were able to grow.

Additional Data on Failure Surfaces

In Figure 30, the effect of pressure on strength is shown. Previously, we were unable to generate tensile data due to the restrictions placed upon stress-state through specimen geometry. Using "dumbbell"-shaped tensile specimens, however, the data points indicated by the closed diamonds recently were obtained. Note also that pure tensile data (for P = 0) obtained from biaxial tests on hollow cylinders are included, and that the points agree very well with the value indicated by extrapolating the "dumbbell" data.

On the other hand, the physical meaning of all of the data is not clear, due to the fact that the data at high pressures do not agree with the previous points obtained for $\sqrt{2}$ P > 100 KSI, using uniform cylindrical specimens. In the latter case the specimens had failed at low, but finite compressive stresses, whereas the new data extend the apparent tensile cutoff up to at least $\sqrt{2}$ P = 140 KSI. In order to determine whether specimen geometry might be involved in this discrepancy, a special "dumbbell" specimen having a very large radius (3 in.), so that the specimen shape approached a uniform cylinder, was fabricated and tested at a high pressure ($\sqrt{2}$ P = 140 KSI). The result is shown in Figure 30, and indicates that a geometric effect probably does exist for pressures greater than $\sqrt{2}$ P = 100 KSI.
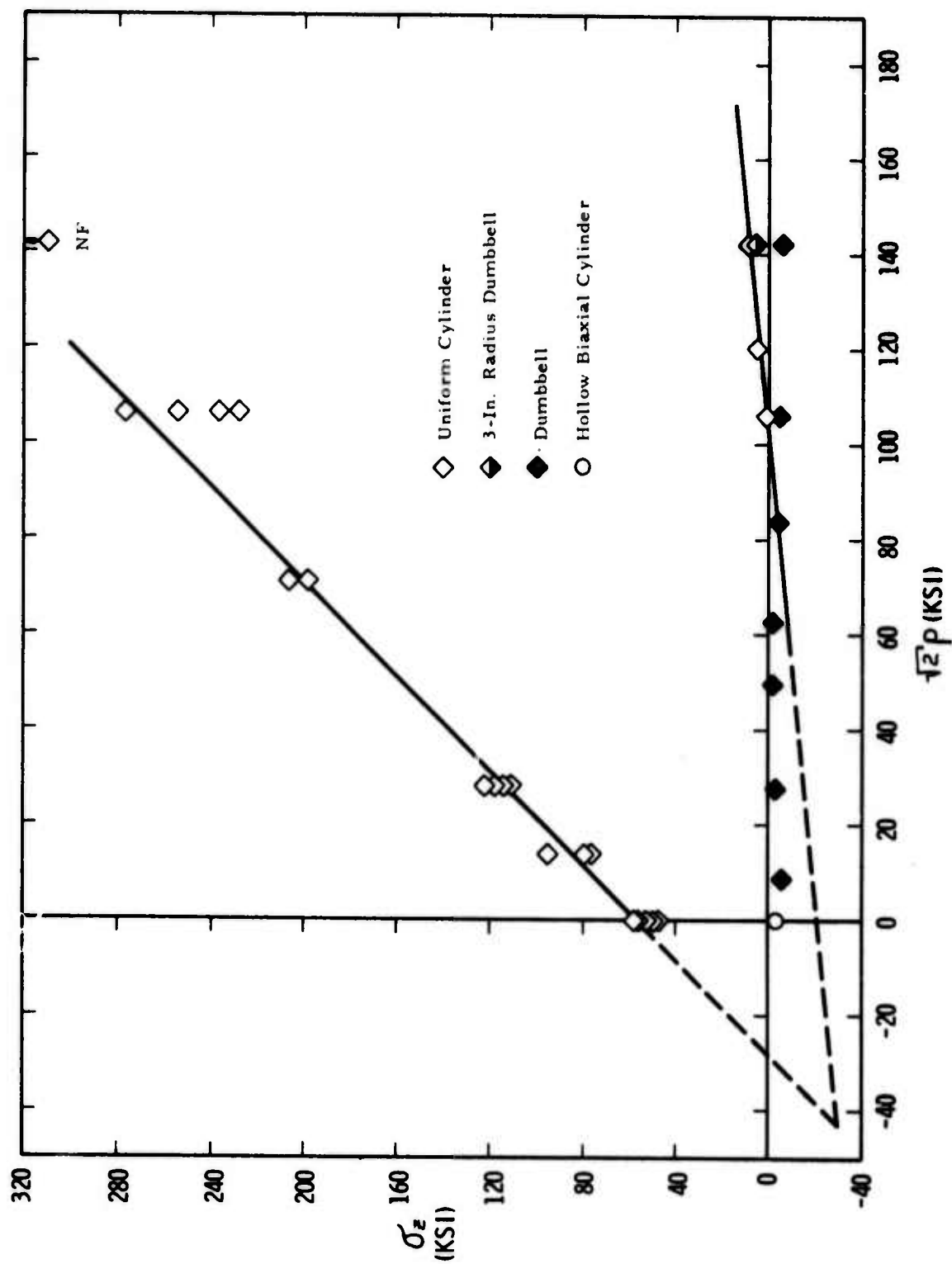
FIGURE 30. FAILURE STRENGTH AS A FUNCTION OF CONFINING PRESSURE

The validity of data obtained from severely undercut specimens is therefore questionable at high pressures.

The shear-axial failure stress data, obtained from hollow biaxial specimens, is presented in Figure 31. The shear stresses shown are the maximum stresses calculated for the outer fiber radius. In order to obtain a preliminary idea of the dependency of biaxial failure upon load-path, two loading schemes were used. In particular, some of the tests involved loading at a constant τ_{xy}/σ_x ratio, while others required loading axially at $\tau_{xy} = 0$, then loading in shear to failure. These paths are shown as dotted lines in Figure 31; apparently the failure envelope was relatively insensitive to the imposed load-paths. Previous data for pure compression are included as different symbols, and seem to agree quite well with the shear-compression data.

It is common to plot such results in the biaxial planes as well. Once this simple algebraic transformation is performed, the plot of Figure 32 is obtained. On the same plot, axial compression-external pressure data (closed circles) obtained using the large hollow ring specimens are included, as are the original[1] uniform cylinder data. All of these results have been normalized, using the average uniaxial compressive strength (53 KSI) as a normalizing factor. These results were utilized in fitting higher order failure theories, since the simple Coulomb-Mohr criterion, shown in the figure, obviously is inadequate in the present case.
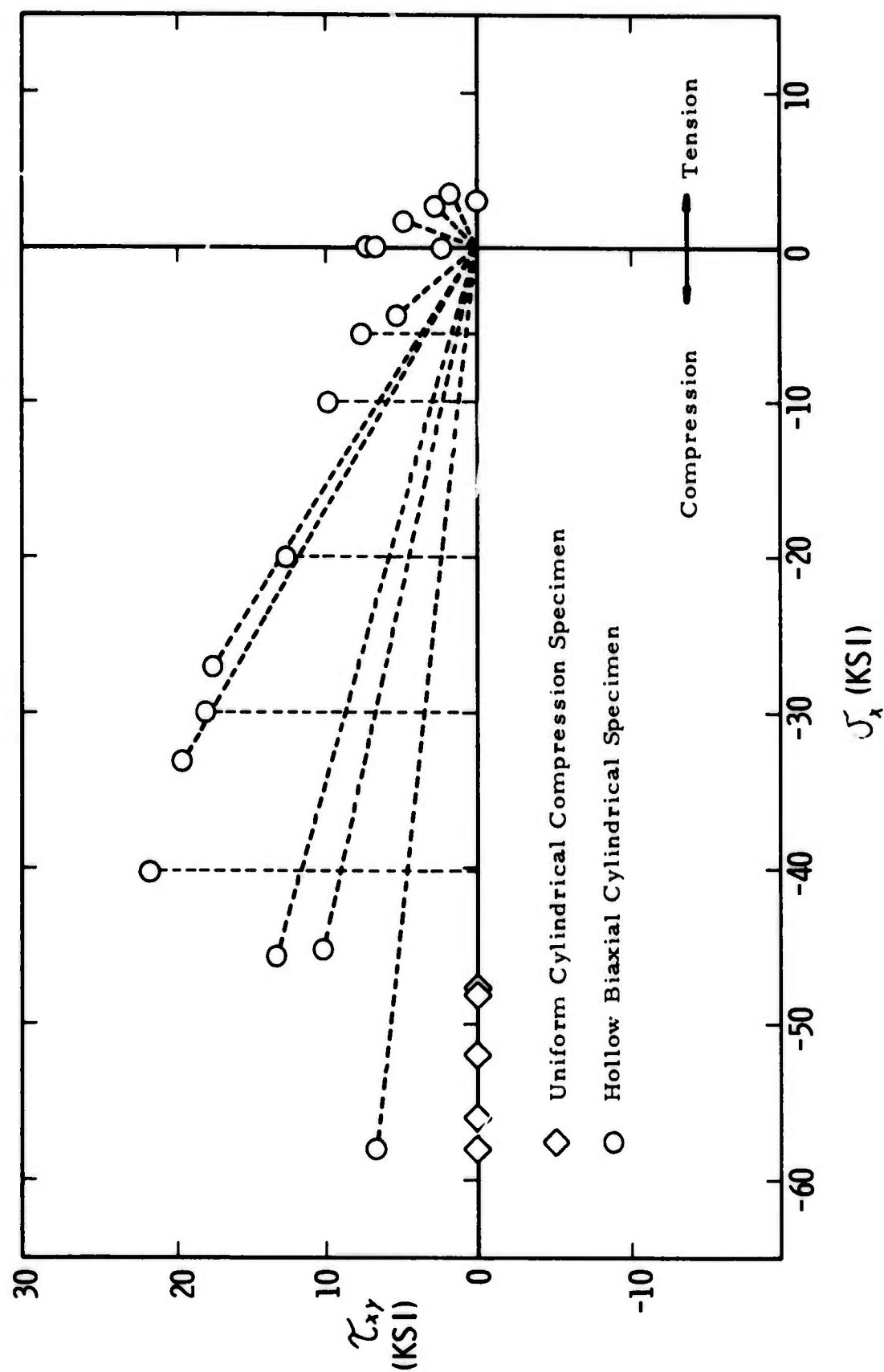
FIGURE 31. BIAXIAL SHEAR-AXIAL STRESS FAILURE ENVELOPE

64
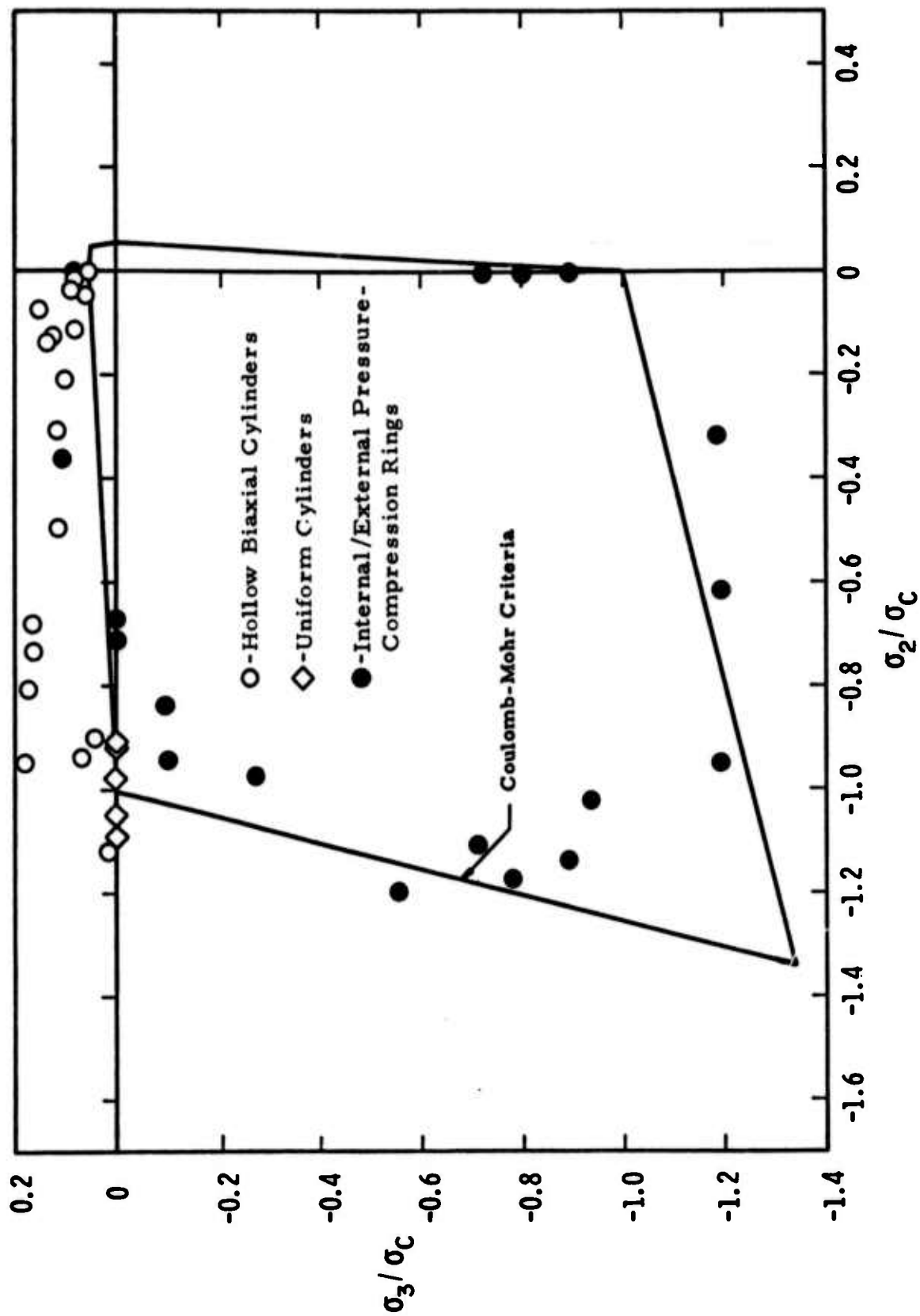
FIGURE 32. FAILURE ENVELOPE IN BIAXIAL PLANE

O - Hollow Biaxial Cylinders
◇ - Uniform Cylinders
● - Internal/External Pressure-
    Compression Rings

Coulomb-Mohr Criteria

σ_2/σ_C

σ_3/σ_C

65

In choosing a higher order criterion, it also was necessary to employ the σ_z - $\sqrt{2}$ P data (Fig. 30), which gives the compressive strength as a function of pressure. The failure surfaces so chosen will be discussed later.

High Temperature Tests

Compressive strength as a function of temperature and strain rate was studied previously[1] up to 800°K. From this earlier work, it appeared that there existed a stress cutoff (σ_0) of ~40 KSI, below which failure was not obtained, irregardless of strain rate or temperature. There remained the question of whether this strength limit would degenerate gradually or catastrophically with higher temperatures.

The results obtained in considering this point are shown in Figure 33. All of the tests above 800°K were performed at a strain rate of 1.9×10^{-4} sec^{-1}, since the strength at the fastest conventional machine strain rate of 2.4×10^{-1} sec^{-1} was down to the cutoff value above 600°K. On the other hand, severe technical difficulties mitigated against instrumenting the Hopkinson bar for high temperature tests in which the strength would have been expected to exceed σ_o. From the figure, it is evident that softening of the rock, and probably localized melting, occurs just below 1400°K. Optical examination of the fracture surface at the highest temperature revealed the presence of numerous tiny, spheroidal particles which were seemingly sintered onto the fracture surface. It should be pointed out that the high temperature point represents something of an anomaly, to the extent that
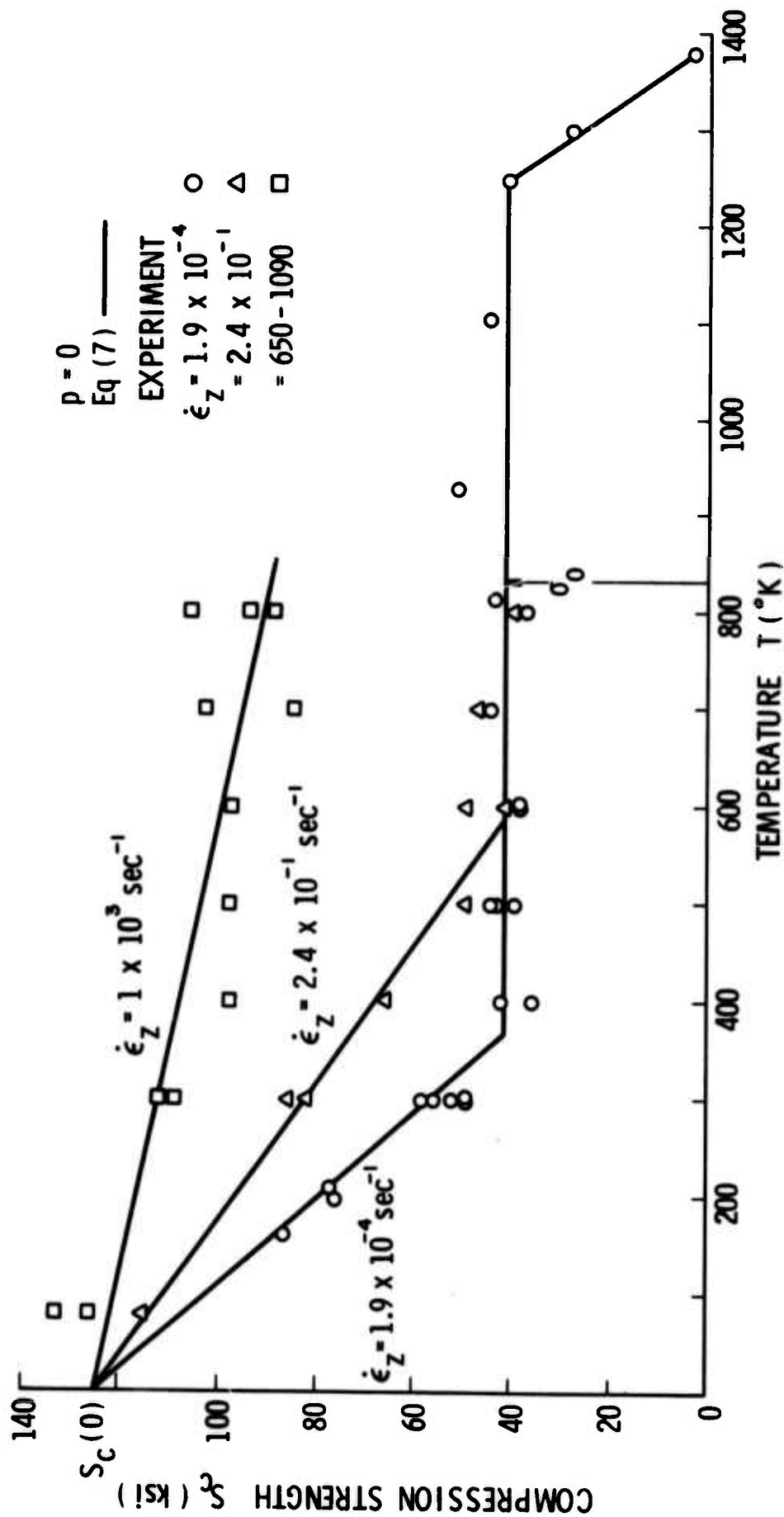
FIGURE 33. EFFECT OF TEMPERATURE AND STRAIN RATE ON
UNCONFINED COMPRESSION STRENGTH

67

the specimen actually crept to failure, rather than breaking under a dynamic load. In all of these tests, a small, ~2,500 KSI compressive preload was applied in order to maintain platen-specimen contact until the specimen had achieved the temperature desired for the dynamic load. In the case just described involving creep, the specimen had been on its way to $1400°K$ when failure occurred.

Strain Distributions Within Specimens

In considering the strain distribution within the uniform cylindrical and the hollow ring specimens, it is expedient to refer back to Figure 32, in which the trace of the failure envelope within the biaxial plane is shown. As mentioned previously, a number of specimens were strain-gaged, and then loaded elastically, usually to a stress level of $\sim\frac{1}{2}\sigma_f$, i.e., 25 - 30 KSI. The solid cylinders were gaged over more than $300°$ at both one end and at the midheight. The hollow ring specimens were instrumented similarly, having two 3/4-in. gages each at one end and two at the midheight positions, each pair being separated by $180°$. It was possible to apply only internal gages, since external pressure was being used to generate a biaxial stress state.

Not surprisingly, some stress paths were found to produce significantly less homogeneous strain distributions than others. The worst cases appeared to be those involving biaxial loading of the ring specimens with $\sigma_2 > \sigma_3$. For such paths in stress space, frictional effects caused by the

68

large axial compressive loads probably compromised the capability of the specimen to contract uniformly. At a stress level of 25 KSI, strains at end and midheight often disagreed by as much as 200 μin/in. On the other hand, in some regions of stress space, deformation was extremely homogeneous. Figure 34 shows a plot of circumferential strain versus circumferential stress (σ_3 in biaxial stress space) for all four strain gages of a specimen loaded in pure radial compression, i.e., along the $\sigma_2 = 0$ axis. It is apparent that the four gages agree, at a given stress level, within a few microstrains. Two load-unload cycles were run, and the agreement was excellent. Agreement was still good, but progressively worse, as the axial stress component σ_2 increased. It was considered that the assumption of strain homogeneity was reasonably valid until the bisector of the $\sigma_2/\sigma_C - \sigma_3/\sigma_C$ axes was reached. Interestingly enough, however, one other set of homogeneous deformations was observed. These were the data for uniaxial compression of the solid cylinders (diamonds along $\sigma_3 = 0$ axis). Figure 35 shows the $\sigma_z - \epsilon_\theta$ response as monitored by circumferential strain gages located at one end and the midheight. At a stress as high as 30 KSI, the gages agree within 50 μin/in.

In view of the above, it is probably valid to delete some of the experimental data from consideration when attempting to choose a failure criterion. Consequently, the hollow ring data for the octant $\sigma_2 > \sigma_3$ was deleted, and the $\sigma_2 > \sigma_3$ data were reflected about the σ_2/σ_3 bisector in order to provide a smooth curve defining P (the ultimate equi-biaxial compressive strength).
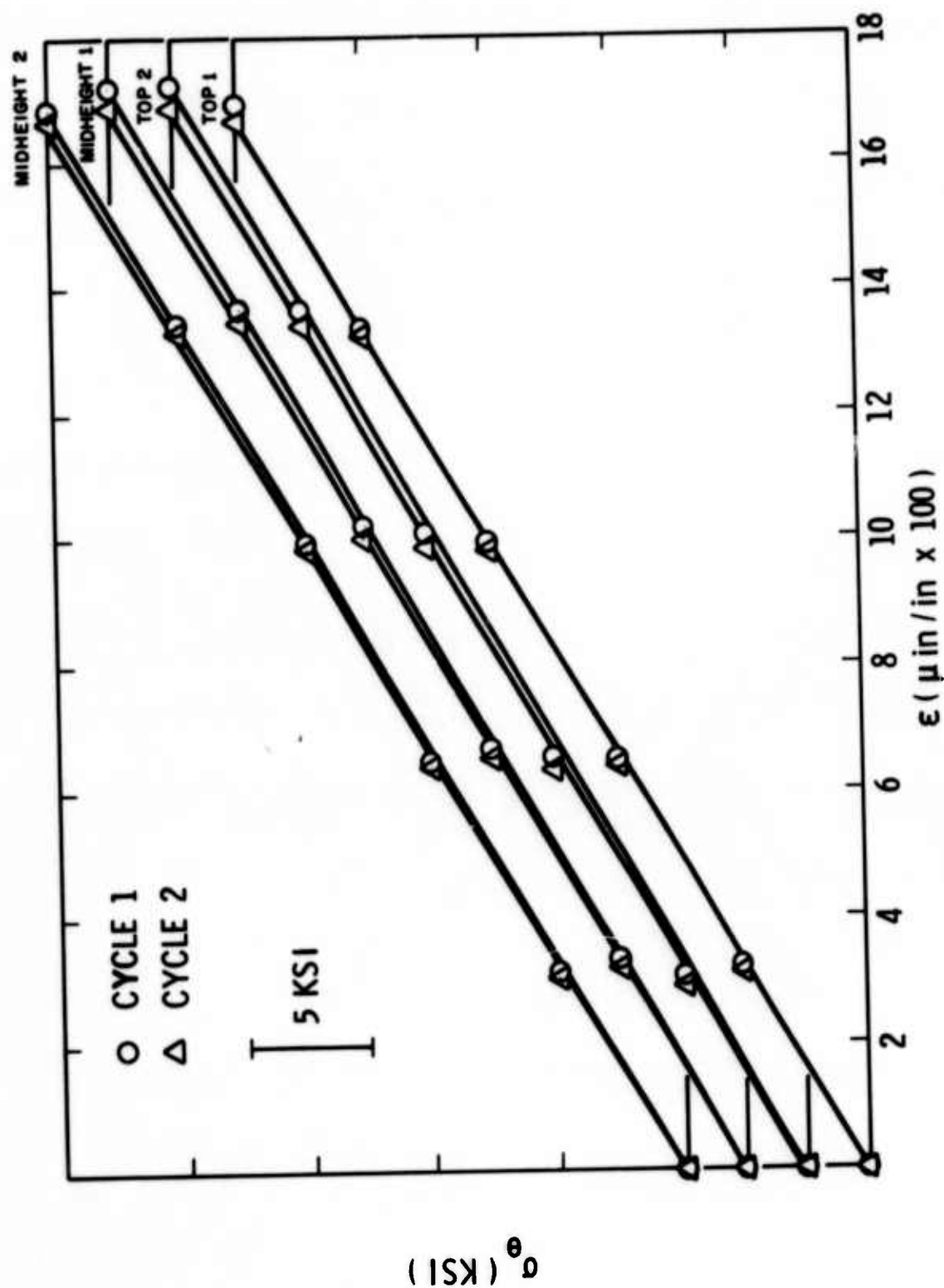
FIGURE 21. CIRCUMFERENTIAL STRAIN VERSUS CIRCUMFERENTIAL STRESS
FOR PURE RADIAL COMPRESSION

70
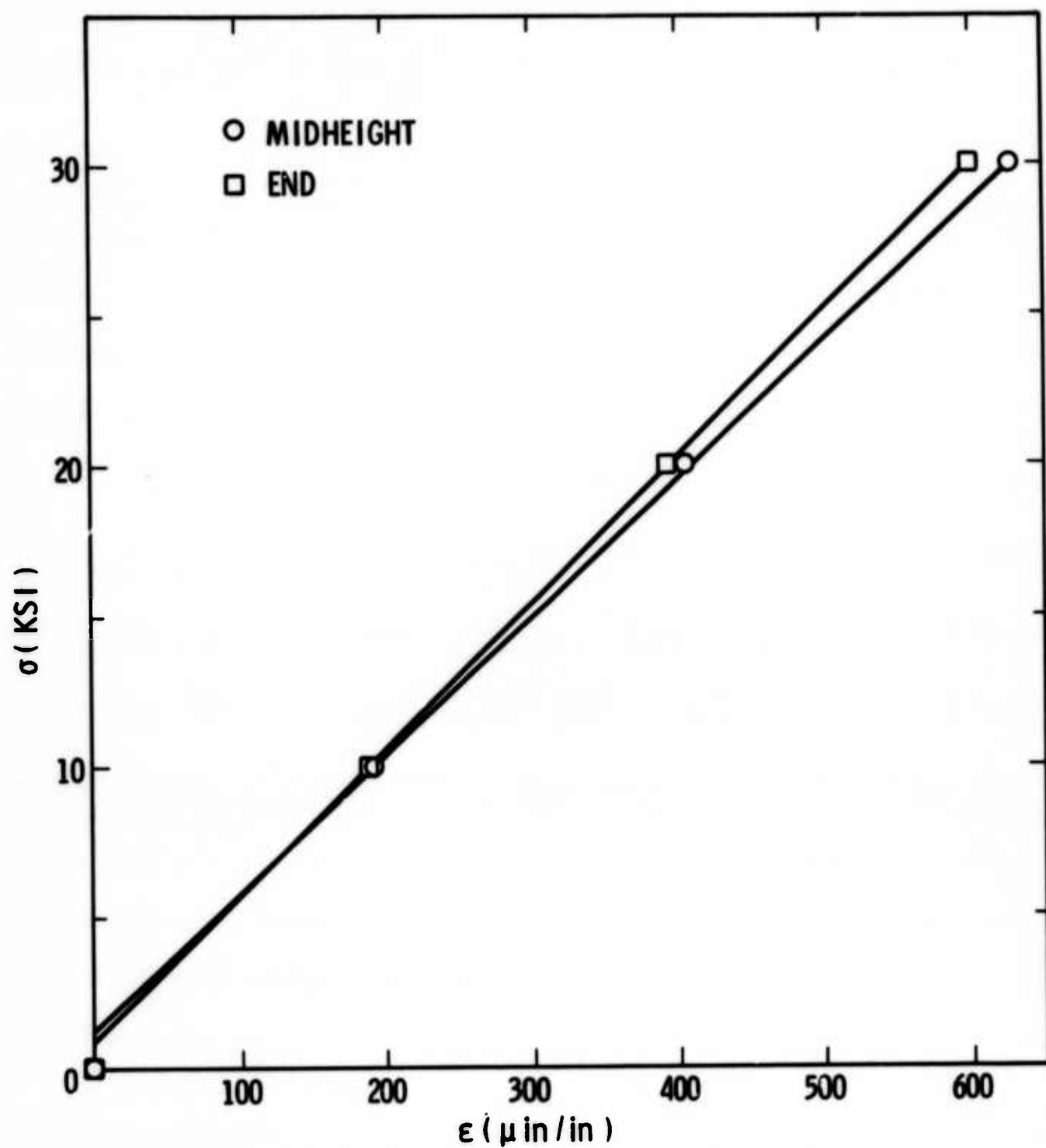
FIGURE 35. AXIAL STRESS VS CIRCUMFERENTIAL STRAIN
FOR PURE UNIAXIAL COMPRESSION

71

Creep Tests

The results of the creep tests described previously are shown in Figure 36. It is emphasized that all of the points shown do represent some sort of creep; i.e., the machine was stopped and the load stabilized for even the shortest lifetimes. The cross-hatched region represents the envelope of failure stress and times to failure for many specimens loaded at a constant strain rate of 1.9×10^{-4}. The variation in these results may reflect the variation in defect structure which must exist prior to unstable fracture. Based on the constant strain rate tests discussed earlier, it seems reasonable that whatever accounts for the variation in stress level from the Stage II-Stage III transition quite likely may be related to the large scatter in creep lifetime at the various stress levels. Furthermore, no macroscopic "flaw" was identified with failure under conditions of constant imposed strain rate. Instead, the "flaw" consisted of an arrangement of microfractures unique to each specimen, as in the constant strain rate tests. The uniqueness involved the size, orientation, and distribution of the microcracks, and produced scatter in failure strength because of the different stress levels required before coalescence into faults could commence. The principal benefit to be derived from these few tests is that in terms of apparent macrofracture behavior, creep failure and dynamic failure are qualitatively similar.

Failure Envelope for $\dot{\epsilon} = 1.9 \times 10^{-4}\ sec^{-1}$

σ_z (KSI)
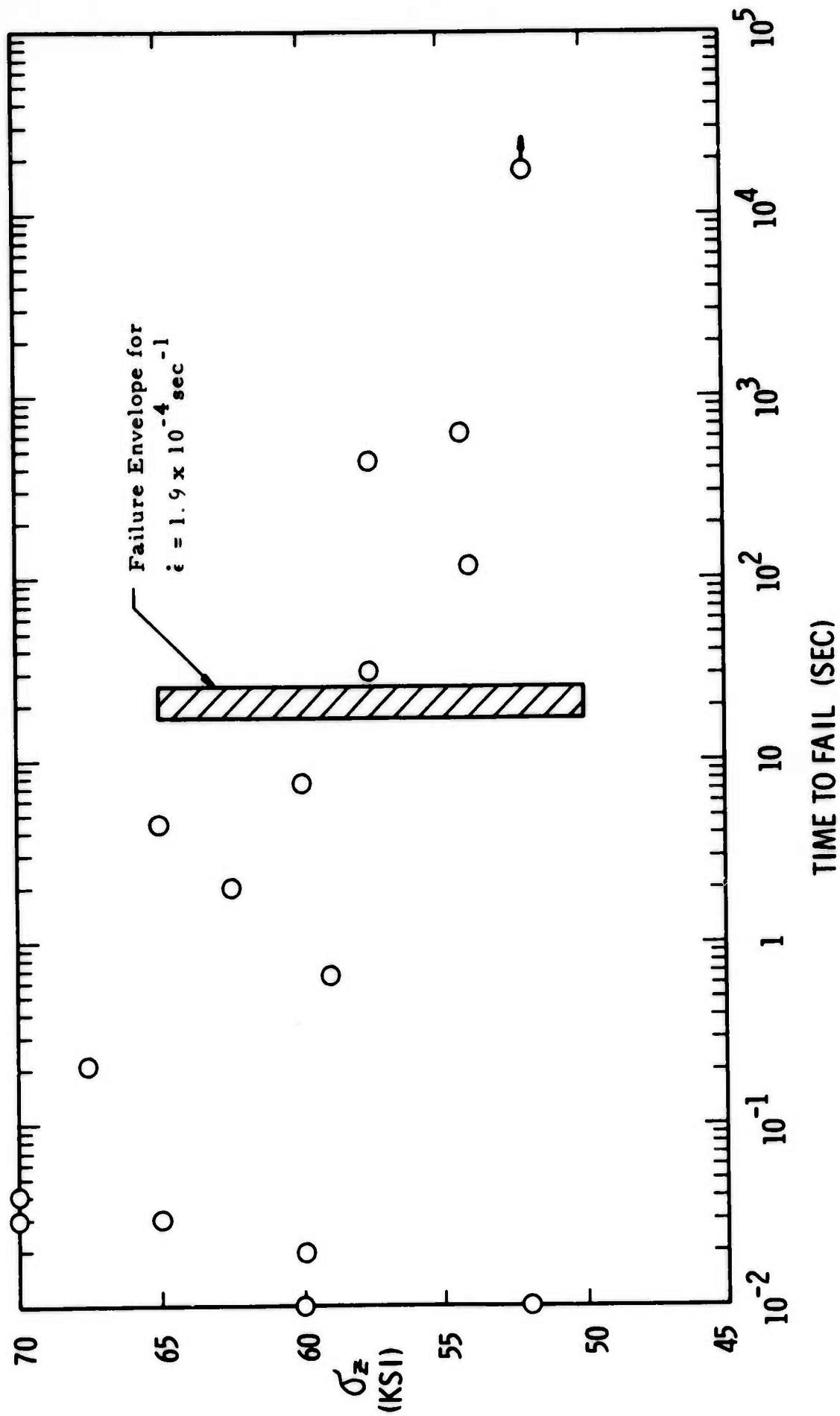
TIME TO FAIL (SEC)

FIGURE 36. CREEP TIME TO FAILURE AT VARIOUS STRESS LEVELS

DISCUSSION

Failure Criteria

Strength to failure data for the $\sigma_2^* \sigma_3^*$ plane, which contains the space diagonal, are shown plotted in Figure 37. Four types of specimen configurations (solid cylinder, 3-in.-radius dumbbell, small radius dumbbell, and hollow biaxial cylinder) were used in obtaining these data points. Because of the nonsymmetrical nature of the data points' distribution in the $\sigma_2^* \sigma_3^*$ plane with respect to the hydrostatic vector (σ_3^* axis), and also due to the fact that the failure strength varies nonlinearly with confining pressure, all prismatic limit surfaces, pyramidal limit surfaces, and limit surfaces of revolution (with respect to σ_3^* axis) are inadequate for fitting the data. The only physically reasonable limit surfaces left are the Mogi, Priddy and the Hexa-Paraboloidal limit surfaces. In Figure 37 the Mogi and Priddy criteria have been used to fit the data. Both of the limit surfaces are forced to pass through points σ_T = 3.2 ksi, σ_C = 53 ksi, and P = 61 ksi (P has been defined previously). It appears that the Mogi criterion fits the data somewhat better than the Priddy criterion. For $\sqrt{2} P > 80$ ksi, the small radius dumbbell data were considered unreliable, as discussed earlier, and these points indeed fell outside of the Mogi failure surface.

74
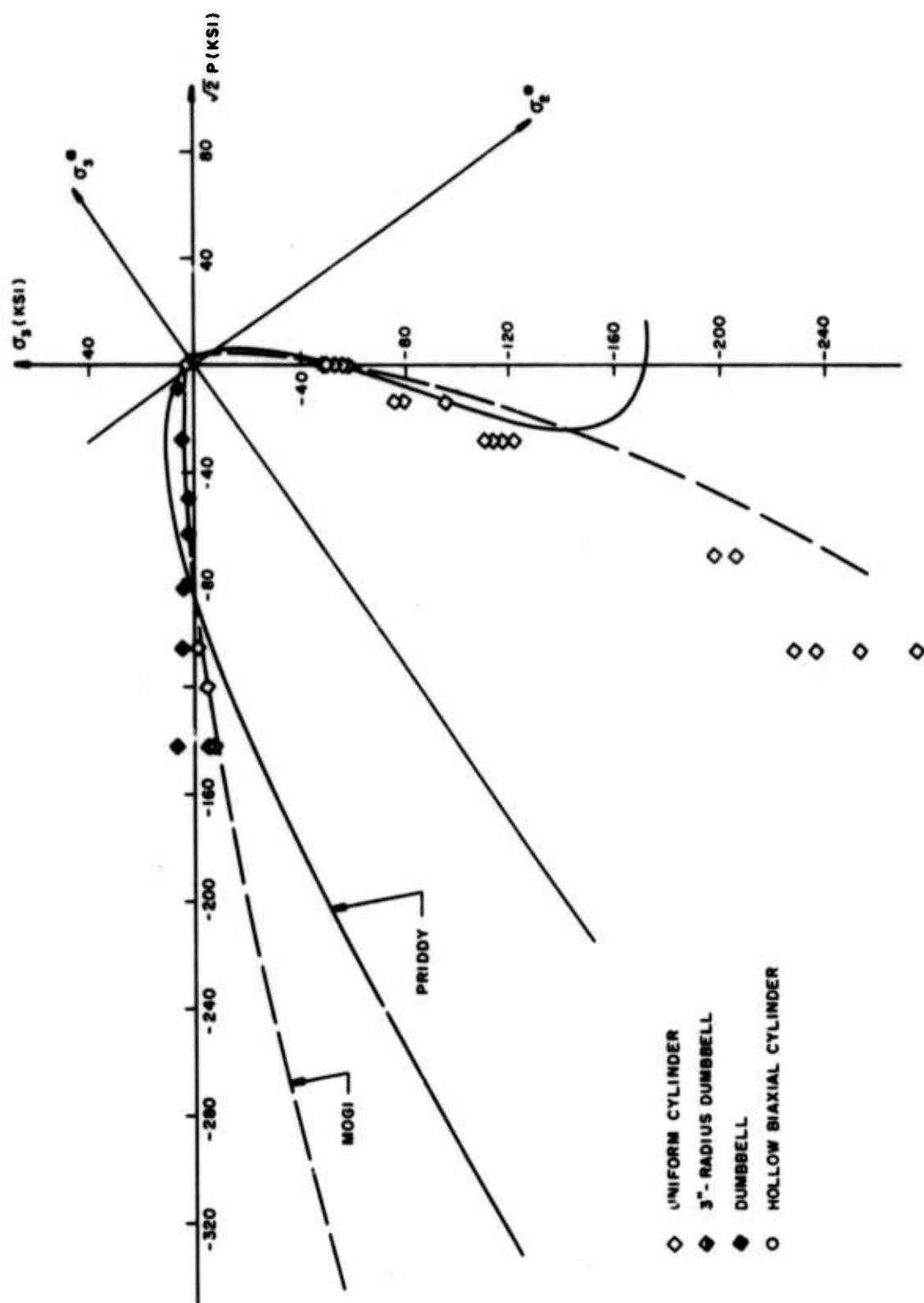
FIGURE 37. FAILURE ENVELOPE IN $\sigma_2^* \sigma_3^*$ PLANE

Figure 38 shows the failure strength distribution within the $\sigma_1 \sigma_2$ plane. In this case, the data were obtained from tests on three types of specimens (solid cylinder, hollow biaxial cylinder and hollow ring), and were normalized in terms of $\sigma_C = 53$ ksi. In the third quadrant of the figure, only the reliable data shown in the $\sigma_2 \sigma_3$ octant third quadrant of Figure 32 are used, as discussed earlier. The Mogi and Priddy limit loci (the cross sections respectively of the Mogi and Priddy limit surfaces passing through $\sigma_T = 3.2$ ksi, $\sigma_C = 53$ ksi, and $P = 61$ ksi) are shown in the figure for comparison with the data. In this plot, Mogi criterion clearly fits the data better than the Priddy criterion.

Microfracture Mechanisms

Based on study of uniaxial, unconfined compression data, it appears that the deformation of Dresser basalt is essentially elastic (Stage I) below a stress level of 20 KSI. If one takes as a definition of the elastic limit the appearance during stress cycling of the first σ-ϵ hysteresis loop, then the true limit probably is on the order of 12-15 KSI. According to Walsh,[42] the elastic region generally corresponds to two separate processes: (1) elastic distortion of the mineral grains and (2) shifting and sliding of grains (along grain boundaries). From extensive study of replicas taken from specimens loaded below 20 KSI, we have observed no evidence of such grain boundary sliding in Dresser basalt.

It has been suggested[12] that the onset of the first nonlinear stage (Stage II, wherein $n \simeq 2.5$) corresponds to continued elastic distortion of

76
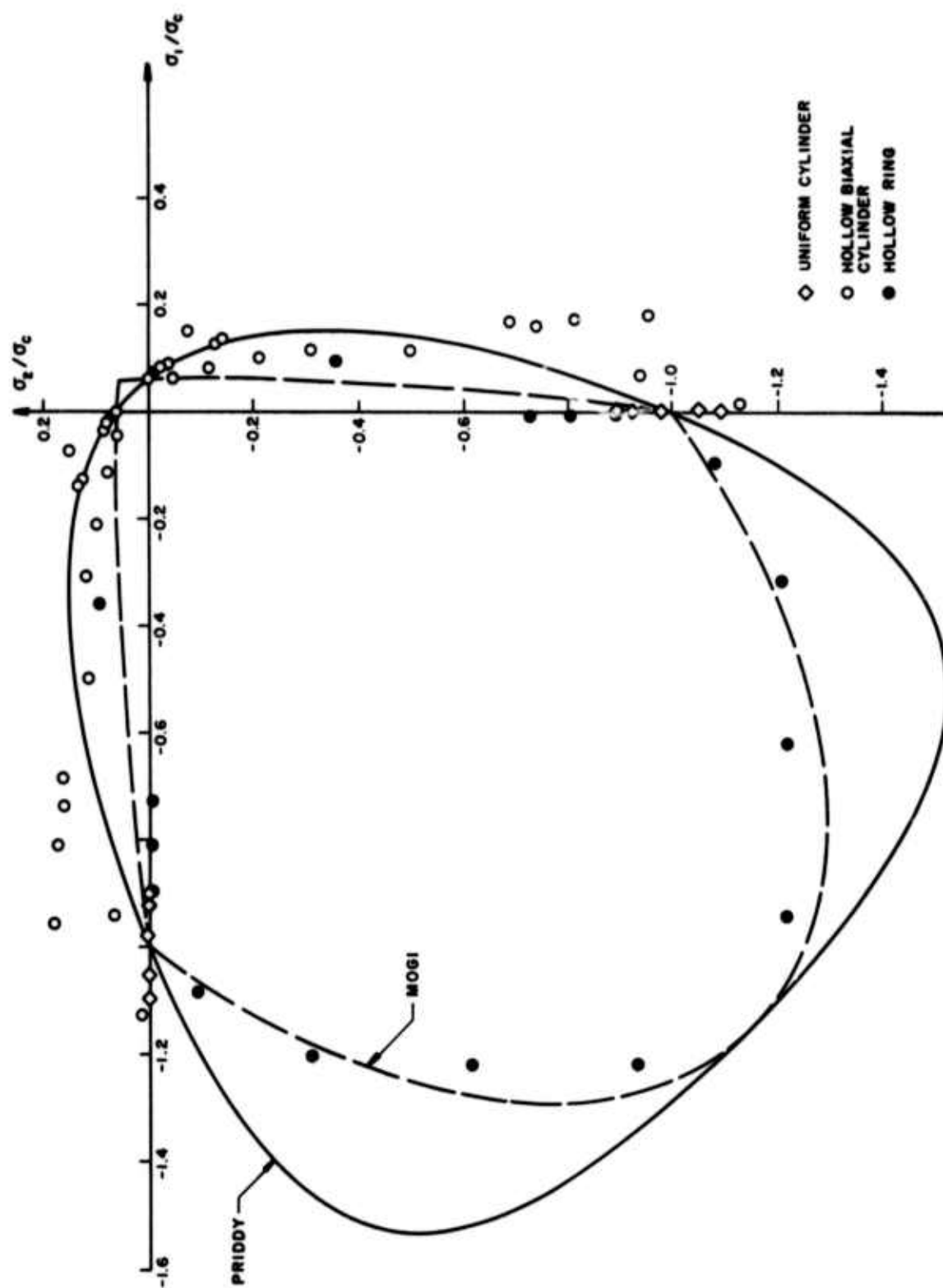
FIGURE 38. FAILURE ENVELOPE IN $\sigma_1\sigma_2$ PLANE

77

grains, further frictional grain boundary sliding, and the formation of open axial cracks. However, the results of the present study give a somewhat modified view of the deformation processes in this region. First, it has been shown[43] that for the classical problem of interfacial slip damping during sliding friction, $\Delta E \propto \sigma^{3.0}$. The closeness of this relation to our experimental result of $\Delta E \propto \sigma^{\sim 2.5}$ indicates that the primary energy dissipative mechanism probably is crack sliding, modified by some secondary hysteresis process. From study of replicas taken during Stage II, this process appears to be the initiation of intragranular microcracks, oriented both axially and at a shear angle to the applied compressive stress. No grain boundary sliding or cracking was observed. The observation of microcracks per se within this region, and the suggestion of dilatancy, is strongly supported by the gradually increasing areas of successive $\sigma - \dfrac{\Delta V}{V_0}$ hysteresis loops within Stage II. In particular, Walsh[42] has shown theoretically that the formation of void areas caused by crack sliding will necessarily produce stress-volumetric strain hysteresis.

Most theories of fracture in rock have been based upon the assumption that grain boundary cracks, both pre-existing and deformation induced, are the defects responsible for failure. For certain rocks, this idea probably is valid. However, the results of the present study agree more closely with the general findings of the recent study of granite and diabase by Wawersik and Brace,[21] who concluded that the above concept of the importance of grain boundary cracks may require revision. They observed

that at least 50% of all cracks are intracrystalline, and are not located along grain boundaries, and further, that inclined cracks are capable of propagating in their initial plane rather than into the direction of greatest compression. [44,45] The present findings concur with these observations. Furthermore, it is quite doubtful that many observed grain boundary openings are at all significant, if for no other reason than their geometry. Brace, et al., [22] recently have observed that for the majority of such cracklike cavities, sharp ends are the exception rather than the rule. Usually these cavities are not interconnected, and they are not generated through brittle processes. Thus, whereas they may serve as local stress concentrators, they do not appear to play an active role during early crack formation. It is partly for this reason that reliance in the present work has been placed upon observing the nucleation, growth, and coalescence of surface cracks, rather than upon thin section observation, in which many of the observed "cracks" may be merely pre-existing grain boundary pores.

With continued cycling in Stage II, more intragranular cracks are formed, and a few of the old ones grow. The ones that grow frequently end at grain boundaries. At some critical stress level (~80% of what will ultimately be the failure stress), something happens which causes greatly increased irreversible energy loss, and a decreased rate of strain ("crack"?) hardening. From microscopic study, this point (the beginning of Stage III in Figure 17, arrows in Figure 21) appears to correspond to either (1) onset of stable growth of microcracks which had initiated within and had

79

portions of grain interiors, and been blocked from further growth by grain boundaries or other defects, or (2) breaking "bridges" separating intragranular cracks lying on roughly parallel but offset fault planes. One possibility is that the energy absorption transition represents passage from a predominantly crystallographic mode of cracking to a partially non-crystallographic mode, and that the latter is a higher energy process. Crack initiation and propagation is confined almost exclusively to feldspar and pyroxene. It has been established that both possess planes of good cleavage, and feldspar usually contains numerous lamellar twins. If the joining of neighboring transgranular, crystallographic cracks requires fracture along non-cleavage planes, it would be reasonable to expect a larger irreversible energy loss related to the creation of the new interface than had previously been required to produce an equal cleavage interfacial area.

Two considerations lend further credence to the general model described above. First is the fact that Stage III energy dissipation is a stress-history dependent process, as evidenced by the decreased hysteresis loss upon cycling at stresses equal to the most recently achieved flow stress (Figure 21, a and b). Secondly, this behavior correlates quite well with the acoustic emission results of Scholtz, [13] in which the emission caused by microfracturing, as opposed to that due to stable hysteretic sliding, increased dramatically, in granite, at some stress greater than 50% of the failure strength. Brace, et al., [12] conclude independently that the stress to cause new Stage III cracking should increase with each cycle to a higher

stress, which would indeed imply reduced hysteretic loss, i.e., due to frictional sliding alone, until the higher stress required for further crack growth is achieved.

Considering the fact that crack initiation is observed at very low stresses, it does appear that the thermally activated process must be related to crack growth. This is reflected in the fact that the transition in energy absorption is pushed to extremely high stresses (Fig. 21) at $77^\circ K$, as compared to the much lower transition stress level for room temperature deformation. The question that remains is whether the thermally activated process primarily affects the extension of families of axial cracks, or rather subsequent "bridging" in order to coalesce such a family into a fault. Some insight into this question may be obtained by considering the temperature-strain rate data generated earlier in the program.

Thermally Activated Processes

In an earlier report,[1] it was shown that the failure stress for Dresser basalt could be described by a relation of the form

$$\sigma_f = \frac{U_o}{v} + \sigma_o - \frac{RT}{v} \ln \left(\frac{\dot{\epsilon}_o}{\dot{\epsilon}} \right)$$

where σ_f is the applied stress of failure, T is the temperature, $\dot{\epsilon}$ the strain rate, v the activation volume, and U_o the total activation energy of the fracture process. $\left(U_o/v \right) + \sigma_o$ is the limiting stress at T = 0, or for $\dot{\epsilon} = \dot{\epsilon}_o$. From the actual failure stresses at various temperatures and strain rates, the apparent activation energy was found to be 2,600 cal/mole, while the

81

activation volume was 3.15×10^{-23} cm^3 (or, approximately, a cube measuring about 3 $\overset{\circ}{A}$ on a side). Similar values for activation energy to failure under dynamic loading conditions were previously obtained by Kumar[4] for a weaker basalt (U_o = 750 cal/mole) and by Serdengecti and Boozer[3] for Pala gabbro (U_o < 1000 cal/mole).

In order to evaluate the physical significance of these activation energies, it is instructive to consider the work of certain other experimenters, involving (1) creep, and (2) the effect of environment. Earlier, Misra and Murrell[8] studied creep of microgranodiorite compressed at several temperatures. From tests run at temperatures of 293°K and 793°K, an activation energy of ~3 kcal/mole was obtained. However, data taken at 793°K and 903°K gave an activation energy of 18 kcal/mole. Similarly, Rummel[9] conducted creep tests of granite loaded in uniaxial compression at temperatures of 290°, 373°, 473°, and 673°K. The activation energy derived from the 290°K to 473°K tests was 2.8 kcal/mole, while the 473°K to 673°K tests gave a value of 10.2 kcal/mole. Eaton[10] calculated an activation energy of 35 kcal/mole from creep tests of dunite within the range of 973°-1273°K. From these results, it appears that there is a trend toward higher apparent creep activation energies with higher temperatures. All of the data discussed above are summarized in Table I.

Another important set of experiments relevant to the present work was carried out by Krokosky and Husak,[17] who investigated the effect of normal atmospheric conditions upon the strength of basalt. The reference,

82

TABLE I. SUMMARY OF DATA ON THERMALLY-ACTIVATED FAILURE OF ROCK AT ATMOSPHERIC PRESSURE

Material	Type of Loading	Temperature Range (°K)	U_o (kcal/mole)	σ_{FS} $(\epsilon \leq 10^{-4})$ (KSI)	σ_{FF} $(\epsilon = \epsilon_o)$ (KSI)	$\dfrac{\sigma_{FF}}{\sigma_{FS}}$	Reference
basalt	dynamic	77-300	0.75	28	75	2.67	Kumar[4]
Westerly granite	dynamic	300		~37	~75[2]	2.0+[2]	Green, et al.[46]
Pala gabbro	dynamic	300-420	<1.0	~30	--	--	Serdengecti & Boozer[3]
Dresser basalt	dynamic	77-400[1]	2.6	58	125	2.16	Lindholm, et al.[1]
Micrograno-diorite	creep	293-793 793-903	3.0 18.0	--	--	--	Misra & Murrell[8]
granite	creep	290-473 473-673	2.8 10.2	--	--	--	Rummel[9]
dunite	creep	973-1273	35.0	--	--	--	Eaton[10]

1. Data were taken at higher temperatures, but for calculating U_o, the temperature range $T \leq 400°K$ was used, since the strength showed essentially no change for the slowest strain rates at $T > 400°K$.

2. Temperature was not varied from $300°K$, so σ_{FF} here corresponds to $\dot{\epsilon} = 10^3$, and is therefore probably slightly low.

uncontaminated condition involved testing under ultra-high vacuum at a slow strain rate following a vacuum bakeout. In effect, moisture was removed as a test variable, and the result was an approximate doubling in the failure strength of the rock. Specifically, the average strength under ambient conditions (σ_{FA}) was 16.3 KSI, while baking-out and testing under vacuum gave σ_{fv} = 30.4 KSI. It is generally accepted that moisture affects fracture in brittle solids through some sort of stress corrosion mechanism; diffusion may or may not be involved.

Now, another way to "eliminate" a thermally activated process is to simply exceed the maximum rate at which the process may proceed. This has essentially been done in the dynamic loading experiments mentioned earlier, as shown in Table I. In these cases, the failure stress at the slowest strain rate and T = 293°K (σ_{FS}) is compared with that corresponding to the extrapolated strength at an infinitely fast strain rate, σ_{FF}. Such a rate is approximated fairly well by rates on the order of $\dot{\epsilon} = 10^3$ sec^{-1}. It is especially interesting to consider the quantity σ_{FF}/σ_{FS}, i.e., the factor by which the dynamic strength is increased due to suppression of the thermally activated process. On the average, σ_{FF}/σ_{FS} turns out to be slightly larger than 2.0, which agrees rather well with the corresponding vacuum/ambient environment strength ratio of Krokosky and Husak,[17] i.e., σ_{Fv}/σ_{FA} = 1.90. The implication, of course, is that for silicate rocks at $T \lesssim 0.5\ T_M$, where T_M is the melting temperature, failure depends strongly upon some thermally activated environmental

84

process having a low activation energy. The magnitude of the measured activated energies (0.75-3.0 kcal/mole), as well as the extremely small activation volume, essentially one molecular volume, indicates that the activated process probably is some sort of surface interaction. At higher temperatures, a process characterized by a higher activation energy controls fracture. It has been suggested[47] that in this region, ionic diffusion of constituent mineral ions, most likely sodium, is the rate controlling process. Typical activation energies for self diffusion are believed to range from 25-90 kcal/mole.

Throughout the preceding discussion, it was implicitly assumed that microfracture processes associated with creep, i.e., crack growth under static load and/or accumulation of plastic strain under static load, are controlled by the same general types of thermally activated mechanisms which operate during dynamic compressive failure. This point is debatable, but the assumption seems reasonable in light of the available evidence.[15] Recalling the creep experiments performed under the present program, it did appear that microfracturing under both creep and dynamic strain produced macroscopically equivalent failures.

It has been implied throughout that no plastic flow-type deformation was involved. In fact, scanning electron microscopy of pre-polished, deformed specimens reinforced the concept of failure as a purely crack-controlled process. There were no observations of the kinds of surface

damage, such as slip bands or deformation twins, which might be con-strued as resulting from dislocation-type plastic flow.

Another less obvious assumption also was involved in the treatment of the experimental results, namely, that tests run at higher temperatures are basically equivalent to those run at low temperature, in terms of the baseline crack network or Griffith defect structure. This point was very kindly drawn to the attention of the authors by Professor C. Scholz, [48] who suggested rechecking the low temperature strength of specimens pre-viously subjected to the same thermal treatment as those failed at high temperature. If dilatational cracking during the requisite thermal cycling either introduced, or extended existing, Griffith cracks, the result would be an effective lowering of the apparent activation energy to failure. There-fore, several specimens were gradually heated to $800°K$ within a vacuum furnace, but in air. After resting at temperature for five minutes to simu-late the time required for running an actual test, the vacuum system was turned on, and simultaneously the furnace was turned off. The specimens were then allowed to furnace cool in vacuo, after which time they were tested at $300°K$ at a strain rate of $\sim 2 \times 10^{-1}$ sec^{-1}. The strength for three tests averaged 80 KSI, agreeing with the earlier data (no thermal cycle) within 4%. Almost identical results were obtained with specimens which underwent the thermal cycle, but were under vacuum at all times during the cycle, and subsequently were tested at room temperature. On the other hand, the thermal cycle with no vacuum at any point weakened the

86

rock by a factor of ~25%, when these specimens were tested at room temperature. In this case, the prolonged exposure to high temperature during the long cooling down period had allowed the rock to oxidize severely; the color changed from green to orange. While an interesting observation, this effect would be pertinent only in creep experiments run at high temperatures. No such tests were involved in this program, or in any of the creep tests by other workers[8-10] cited in support of the present conclusions.

The point involved in the above experimental check is very important, namely, that activation energies calculated from specimens heated above room temperature are not affected by any cracking which may be related to thermal dilatation. This is not to say that such cracking may not occur; in fact, it probably does take place. Irregardless, the activation energies obtained apparently do reflect in a physically valid way the thermally activated process responsible for controlling the strength of the rock. Mechanically induced cracks therefore appear to be more detrimental to the integrity of the specimen than are those caused by thermal excursions. Furthermore, since the apparent activation energies tend to be small, it seems more likely that the activated process involves some sort of localized stress-corrosion reaction at the tips of axial cracks propagating along cleavage or twin planes, rather than the bridging between such planes, which is expected to be a higher energy process. Further work is needed in order to clarify this idea.

87

REFERENCES

1. U. S. Lindholm, L. M. Yeakley, and A. Nagy, "A Study of the Dynamic Strength and Fracture Properties of Rock," Final Report, Contract No. H0210036, Southwest Research Institute, San Antonio, Texas, August 1972.

2. B. Paul , "Macroscopic Criteria for Plastic Flow and Brittle Fracture," Fracture, Vol. 2, H. Liebowitz, Ed., Academic Press, New York, 315, 1968.

3. S. Serdengecti and G. D. Boozer, "The Effects of Strain Rate and Temperature on the Behavior of Rocks Subjected to Triaxial Compression," Proc. 4th Symp. Rock Mech., Penn. State Univ., 83, 1961.

4. A. Kumar, "The Effect of Stress Rate and Temperature on the Strength of Basalt and Granite," Geophysics, Vol. 33, 501, 1968.

5. S. J. Green and R. D. Perkins, "Uniaxial Compression Tests at Strain Rates From 10^{-4}/Sec to 10^4/Sec on Three Geological Materials," Proc. Tenth Symp. on Rock Mechanics, May 1968.

6. R. D. Perkins, S. J. Green, and M. Friedman, "Uniaxial Stress Behavior of Porph ritic Tonalite at Strain Rates to 10^3/Second," Int. J. Rock Mech. Min. Sci., Vol 7, 527, 1970.

7. W. S. Brown, S. R. Swanson, and W. R. Wawersik, "Influence of Dynamic Loading, Biaxial Loading, and Pre-Fracturing on the Stress-Strain and Fracture Characteristics of Rocks," Final Report, DASA-2713, Univ. Utah, 1971.

8. A. K. Misra and S. A. F. Murrell, "An Experimental Study of the Effect of Temperature and Stress on the Creep of Rocks," Geophys. J. Roy. Astron. Soc., Vol. 9, 509, 1965.

9. F. Rummell, "Studies of Time-Dependent Deformation of Some Granite and Eclogite Samples Under Uniaxial, Constant Compressive Stress and Temperatures Up to 400°C," Z. Geophys., Vol. 35, 17, 1969.

10. S. F. Eaton, "The High-Temperature Creep of Dunite," Ph.D. Thesis Princeton Univ., Princeton, N. J., 1968.

Preceding page blank

11. W. F. Brace, "Brittle Fracture in Rocks," State of the Earth's Crust, ed. W. R. Judd, Amer. Elsevier Publ., New York, 110, 1964.

12. W. F. Brace, B. W. Paulding, and C. Scholz, "Dilatancy in the Fracture of Crystalline Rock," JGR, Vol. 71, 3939, 1966.

13. C. H. Scholz, "Microfracturing and the Inelastic Deformation of Rocks in Compression," JGR, Vol. 73, 1417, 1968.

14. C. H. Scholz, "Experimental Study of the Fracturing Process in Brittle Rock," JGR, Vol. 73, 1447, 1968.

15. C. H. Scholz, "Mechanism of Creep in Brittle Rock," JGR, Vol. 73, 3295, 1968.

16. R. J. Martin, "Time-Dependent Crack Growth in Quartz and Its Application to the Creep of Rocks," JGR, Vol. 77, 1406, 1972.

17. E. M. Krokosky and A. Husak, "Strength Characteristics of Basalt Rock in Ultra-High Vacuum," JGR, Vol. 73, 2237, 1968.

18. W. R. Wawersik, "Detailed Analysis of Rock Failure in Laboratory Compression Tests," Ph. D. Thesis, Univ. of Minn., Minneapolis, Minn., 1968.

19. S. D. Peng, "Crack Growth and Faulting in Cylindrical Specimens of Chelmsford Granite," Int. J. Rock Mech. Min. Sci., Vol. 9, 37, 1972.

20. M. Friedman, R. D. Perkins, and S. J. Green, "Observation of Brittle-Deformation Features at the Maximum Stress of Westerly Granite and Solenhofen Limestone," Int. J. Rock Mech. Min. Sci., Vol. 7, 297, 1970.

21. W. R. Wawersik and W. F. Brace, "Post-Failure Behavior of a Granite and Diabase," Rock Mechanics, 3, 1971, 61.

22. W. F. Brace, E. Silver, K. Hadley, and C. Goetze, "Cracks and Pores: A Closer Look," Science, 178, 1972, 162.

23. R. E. Thill, Private Communication, 1973.

24. U. S. Lindholm, "A Study of the Dynamic Strength and Fracture Properties of Rock," Semiannual Technical Report No. 1, Contract No. H0210036, Southwest Research Institute, San Antonio, Texas, March 1971.

25. J. Lankford and U. S. Lindholm, "A Study of the Dynamic Strength and Fracture Properties of Rock," Semiannual Technical Report, Contract No. H0220063, Southwest Research Institute, San Antonio, Texas, December 1972.

26. R. Hill, The Mathematical Theory of Plasticity, Oxford University Press, London, 1960.

27. G. P. Sendeckyj, "On Strength of Composites," ARPA Contract No. F33615-70-C-1016.

28. T. G. Priddy, "A Fracture Theory for Brittle Anisotropic Materials," SC-DR-71-0764, Sandia Laboratories, Albuquerque, New Mexico, November 1971.

29. A. Mehldahl, "A New Graphical Method of Representing Strength Characteristics," Brown Boveri Rev., Vol. 31, 260, 1944.

30. W. L. Ko, "Topology of Failure Surfaces," Part II of "Application of Finite Elastic Theory to the Behavior of Rubber-Like Materials," Ph.D. Dissertation, California Institute of Technology, Pasadena, California, 1963.

31. I. I. Gol'denblat and V. A. Kopnov, "Strength of Glass-Reinforced Plastics in the Complex Stress State," Mekhanika Polimerov, Vol. 1, 70, 1965.

32. A. Malmeister, "Geometry of Theories of Strength" (in Russian), Mekhanika Polimerov, Vol. 2, 519, 1966.

33. A. Nadai, Theory of Flow and Fracture of Solids, McGraw-Hill, New York, 1950.

34. D. C. Drucker, "Limit Analysis of Two- and Three-Dimensional Soil Mechanics Problems," J. Mech. Phys. Solids, Vol. 1, 217, 1953.

35. F. Schleicher, Z. Angew Math. Mech., Vol. 6, 199, 1926.

36. N. W. Tschoegl, "Failure Surfaces in Principal Stress Space," Polymer Symposia, Vol. 32, 239, 1971.

37. C. Torre, "Die Grenzzustande Statisch Beanspruchter Stoffe," Schweiz. Arch. Angew. Wiss. U. Tech., Vol. 15, 1940.

38. Z. Sobotka, "The Cubic Yield Condition for Incompressible Bodies," ACTA Technica CSAV, No. 6, 830, 1967.

39. D. C. Drucker, "A More Fundamental Approach to Plastic Stress-Strain Relations," Proc. 1st U.S. Nat. Congr. Appl. Mech., 487-491, 1952.

40. S. W. Tsai and E. M. Wu, "A General Theory of Strength for Aniso-tropic Materials," J. Composite Materials, Vol. 5, 58, 1971.

41. K. Mogi, "Effect of the Triaxial Stress System on the Failure of Dolomite and Limestone," Tectonophysics, Vol. 11, 111, 1971.

42. J. B. Walsh, "The Effect of Cracks in Rocks on Poisson's Ratio," JGR, Vol. 70, 5249, 1965.

43. L. E. Goodman, "A Review of Progress in Analysis of Interfacial Slip Damping," Structural Damping, J. Ruzida, Ed., ASME, New York, 36, 1959.

44. W. F. Brace and E. G. Bombalakis, "Note on Brittle Crack Growth in Compression," JGR, Vol. 68, 1963, 2.

45. E. Hoek, "Rock Fracture Under Static Stress Conditions," CSIR Report MEG 383, Pretoria, South Africa, 1965.

46. S. J. Green, J. D. Leasia, R. D. Perkins, and A. H. Jones, "Triaxial Stress Behavior of Solenhofen Limestone and Westerly Granite at High Strain Rates," JGR, Vol. 77, 3711, 1972.

47. J. E. Ritter and C. L. Sherburne, "Dynamic and Static Fatigue of Silicate Glasses," JACS, Vol. 54, 601, 1971.

48. C. H. Scholz, Private Communication, 1973.